*J. Fluid Mech.* (1990), *vol.* 220, *pp.* 53–84
*Printed in Great Britain*



# On the stability of circular Couette flow with radial heating

By MOHAMED ALI† AND P. D. WEIDMAN
Department of Mechanical Engineering, University of Colorado, Boulder, CO 80309, USA

(Received 12 October 1989 and in revised form 12 March 1990)

The stability of circular Couette flow with radial heating across a vertically oriented annulus with inner cylinder rotating and outer cylinder stationary is investigated using linear stability theory. Infinite aspect ratio and constant fluid properties are assumed and critical stability boundaries are calculated for a conduction-regime base flow. Buoyancy is included through the Boussinesq approximation and stability is tested with respect to both toroidal and helical disturbances of uniform wavenumber. Symmetries of the linearized disturbance equations based on the sense of radial heating and the sense of cylinder rotation and their effect on the kinematics and morphology of instability waveforms are presented. The numerical investigation is primarily restricted to radius ratios 0.6 and 0.959 at Prandtl numbers 4.35, 15 and 100. The results follow the development of critical stability from Taylor cells at zero heating through a number of asymmetric modes to axisymmetric cellular convection at zero rotation. Increasing the Prandtl number profoundly destabilizes the flow in both wide and narrow gaps and the number of contending critical modes increases with increasing radius ratio. Specific calculations made to compare with the stability measurements of Snyder & Karlsson (1964) and Sorour & Coney (1979) exhibit good agreement considering the idealizations built into the linear stability analysis.

## 1. Introduction

The viscous fluid flow created between differentially rotating coaxial cylinders has provided a fertile testing ground for both linear and nonlinear stability theory. Beginning with the work of Taylor (1923) numerous experimental and theoretical studies on the transitions to and morphologies of supercritical circular Couette flow have appeared. The rich bifurcation diagram presented in the work of Andereck, Liu & Swinney (1986) becomes even more complex when one considers, for example, eccentrically oriented cylinders, superposed axial throughflow or radial heating, particularly in magnetohydrodynamic or non-Newtontian systems. Initial studies on thermally driven circular Couette flow, motivated by technological problems in the cooling of rotating electrical machinery, have been reviewed by Kreith (1968). Because of the high centripetal accelerations involved, early theoretical attacks neglected gravity and usually considered only axisymmetric disturbances in the limit of infinite aspect ratio. Such investigations by Yih (1961), Becker & Kaye (1962), Walowit, Tsao & Di Prima (1964), Bahl (1972), and Soundalgekar, Takhar & Smith (1981) showed that isothermal Taylor cells are destabilized (stabilized) by positive (negative) radial heating gradients across the gap. Roesner (1978) is credited as being

† Permanent address: Helwan University, Faculty of Engineering Technology, El-Mattaria, Cairo, Egypt.

the first to properly include the effect of gravity in the Boussinesq approximation but, like most of his predecessors, considered only axisymmetric disturbances. Roesner's results contrast those neglecting gravity in that isothermal Taylor cells are stabilized by both positive and negative radial heating and his computed stability boundaries exhibit perfect symmetry with respect to the direction of the temperature gradient. There has been a renewed interest in the problem of radially heated rotating flows, partially from a continued effort to enhance the cooling of rotating machinery (Lee & Minkowycz 1989), but also with the aim of understanding and controlling instabilities in nematic liquid crystal systems (Barratt & Zuniga 1984), in chemical vapour deposition processes (Singer 1984) and in the solidification of pure metals (Vives 1988). Numerical studies of the effects of buoyancy on bifurcation phenomena in systems of small-to-moderate aspect ratio have recently been reported by Ball & Farouk (1986, 1987, 1988). Ball & Farouk (1989) also have presented a flow visualization study of buoyancy-induced transitions from a primary flow consisting of steady isothermal Taylor cells in a wide-gap vertical annulus of moderate aspect ratio.

Although many experiments dealing with global heat transfer effects have been reported, those directed towards an understanding of stability and flow morphology are few in number. For large-aspect-ratio geometries we are aware of only two experimental studies sufficiently well-documented that a direct comparison with stability theory can be made. These are the measurements of Snyder & Karlsson (1964) and Sorour & Coney (1979) and even in the latter investigation unreported Prandtl numbers must be estimated. The present endeavour, in fact, was initiated in an attempt to predict the measurements of Snyder & Karlsson (1964) and to understand apparent conflicts with respect to the thermal stabilization of Taylor cells between their work and that of Sorour & Coney (1979). We pursue the infinite-aspect-ratio idealization, assume a uniform temperature contrast across the annular gap formed between vertical concentric cylinders and include rotation of the inner cylinder only. Proper account of gravity is taken within the limits of the Boussinesq approximation, different Prandtl numbers are considered and stability is tested with respect to both axisymmetric and non-axisymmetric (helical) disturbances. Preliminary aspects of this work have been reported by Weidman & Ali (1989) and a full account is given here. Introductory remarks in §2 lead to the mathematical formulation and numerical solution procedure in §3. Computed stability boundaries along with the associated disturbance wave characteristics presented in §4 is followed by a direct comparison of theory with existing measurements in §5. The discussion of results and concluding remarks are given in §6.

## 2. Preliminary remarks

The fluid-filled annulus under consideration and its $(r, \phi z)$ cylindrical coordinate system is sketched in figure 1. Cylinders of radius $R_1$ and $R_2$ at uniform temperatures $T_1$ and $T_2$ are concentrically disposed about the vertical $z$-axis. In finite systems the geometry of the annulus is measured by both the radius ratio $\eta = R_1/R_2$ and the aspect ratio $\Gamma = L/d$, where $d = R_2 - R_1$ is the gap width and $L$ is the height of the cylinders. With $\bar{k}$ the unit vector in the positive $z$-direction, a uniform gravitational field $-g\bar{k}$ is assumed, the inner cylinder rotates at constant angular velocity $\pm\Omega_1\bar{k}$ and the outer cylinder remains stationary. The following brief review of certain aspects of (i) isothermal Taylor–Couette flow and (ii) natural convection in the absence of rotation is provided to recall the mechanisms triggering instability in the

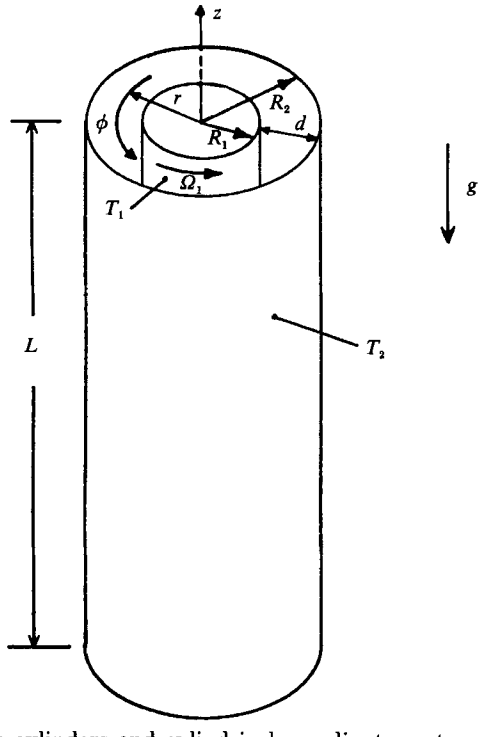


FIGURE 1. Vertical concentric cylinders and cylindrical coordinate system. The outer cylinder is stationary, the inner wall rotates at $\Omega_1$ and the temperature contrast is $\Delta T = T_1 - T_2$.

separate systems, introduce governing non-dimensional parameters, and report results needed for future reference.

The stability of viscous isothermal circular-Couette flow generated by rotation of the inner cylinder is controlled by three non-dimensional parameters: the radius ratio $\eta$, the aspect ratio $\Gamma$, and the Taylor number $Ta = 2\eta^2\Omega_1^2 d^4/\nu^2(1-\eta^2)$, where $\nu$ is the kinematic viscosity of the fluid. At a critical value of the Taylor number the action of *centrifugal* forces leads to an axisymmetric instability consisting of counter-rotating toroidal cells of uniform width stacked one above the other. The Taylor cells have zero phase speed and therefore do not propagate up or down the annulus. Stability predictions derived from analyses in the limit $\Gamma \to \infty$ are borne out by experiments in facilities of sufficiently large aspect ratio that end effects are suppressed. Comprehensive reviews of both theory and experiments on the stability of isothermal circular Couette flow have been given by Di Prima & Swinney (1981), Cognet (1984) and Stuart (1986).

In the absence of rotation, natural convection between vertical differentially heated concentric cylinders depends crucially on the system aspect ratio and the magnitude of the imposed thermal heating. Early experimental studies, starting with the careful investigation by Eckert & Carlson (1961), fostered the identification of three distinct flow regimes in both planar and cylindrical gaps: conduction, transition and convection. The base flow for each of these regimes may be regarded as a single closed cell of fluid rising along the hot wall and descending along the cold wall. For circular cylinders maintained at different uniform temperatures, Thomas & de Vahl Davis (1970) place the *transition* regime in the range

$$400\Gamma < Ra < 3000\Gamma \quad (\Gamma > 5)$$

where $Ra = g\beta d^3\Delta T/\alpha\nu$ is the Rayleigh number, $\Delta T = T_1 - T_2$ the temperature contrast across the gap, $\beta$ the fluid thermal expansion coefficient, $\alpha$ the fluid thermal diffusivity and $g$ is gravity. $Ra < 400\Gamma$ corresponds to the *conduction* regime and $Ra > 3000\Gamma$ corresponds to the *convection* regime where axial boundary layers form along each cylinder wall. Although this criterion delineating the transition regime is reported strictly valid only for unity Prandtl number, the authors claim it is relatively insensitive to both the radius ratio and the Prandtl number $Pr = \nu/\alpha$. Note that infinite aspect ratio immediately implies a conduction-regime base flow, as first noted by Batchelor (1951) for the analogous problem in two dimensions.

Stability for this system is governed by four dimensionless parameters: $G$, $Pr$, $\Gamma$ and $\eta$. Here the Grashof number $G = Ra/Pr = g\beta d^3\Delta T/\nu^2$ is chosen as the control parameter for the imposed radial heating. Numerical calculations by de Vahl Davis & Thomas (1969) and Lee, Korpela & Horne (1982) in finite geometries at $O(1)$ Prandtl numbers with a heated inner wall show the evolution of axisymmetric flow to a multicellular instability which, like the isothermal Taylor instability, is composed of pairs of counter-rotating toroidal cells. These convective instabilities may be distinguished from Taylor vortices by their non-zero phase speed which results in a slow drift of the cellular pattern up the annular cavity. In the limit $\Gamma \to \infty$, an analytical solution for the base flow in the conduction regime is readily obtained. A linearized Galerkin calculation testing the stability of this base flow against axisymmetric disturbances has been carried out by Choi & Korpela (1980). They found that the flow may be driven to instability by *shear* forces for $Pr < 15$ or by *buoyancy* forces for $Pr > 15$, approximately. The distinction between shear-driven and buoyancy-driven instabilities in convective systems of this type is due to Hart (1971). McFadden *et al.* (1984*a*) extended Choi & Korpela's results by testing stability with respect to the first non-axisymmetric disturbance. They report that for air with $Pr = 0.71$ the most dangerous disturbance is helical for radius ratios $0 < \eta < 0.44$ but toroidal for $0.44 < \eta < 1$, and in either case instability is due to the action of shear forces. For water with $Pr = 3.5$ it is shown that the asymmetric shear mode at $Pr = 0.71$ is superseded by an axisymmetric buoyancy-driven instability when $0.03 < \eta < 0.16$. Weidman & Mehrdadtehranfar (1985) have carried out experiments on the stability of natural convection in a vertical differentially heated annulus for base flows in the convection regime, but the only critical stability experiment reported for a conduction-regime base flow seems to be that of Choi & Korpela (1980) done at $Pr = 0.71$, $\Gamma = 38.6$ and $\eta = 0.68$.

The aforementioned high-aspect-ratio experimental studies of Snyder & Karlsson (1964) and Sorour & Coney (1979) focused on the narrow-gap limit and were performed with the inner cylinder rotating and outer cylinder at rest. Snyder & Karlsson obtained measurements for both positive and negative radial heating at $\Gamma = 349$, $\eta = 0.959$ and used water with a reported Prandtl number of 4.35 (but see §5.1). By holding the Grashof number constant and increasing the Taylor number, they found that on the average for $|G| < 40$, the flow is unstable to axisymmetric perturbations, while for $|G| > 40$ spiral cells appear with azimuthal wavenumber increasing with $|G|$. Also, for $|G| < 40$ the system is stabilized with respect to the adiabatic Taylor stability limit $(Ta_c)_0 \equiv Ta_c(G = 0)$, and beyond $|G| \approx 40$ the flow becomes increasingly destabilized to values of $Ta_c$ far below $(Ta_c)_0$. Sorour & Coney performed measurements with a heated outer cylinder at large aspect ratio ($\Gamma \approx 100$) for two gaps at $\eta = 0.911$ and $\eta = 0.948$ using two different oils. Unfortunately, no Prandtl numbers were reported. They observed only axisymmetric instability and, in contrast with the earlier measurements of Snyder & Karlsson, found only

monotonic destabilization of Taylor cells. Sorour & Coney attributed this 'discrepancy' to the existence of a stabilizing density stratification in the experiments of Snyder & Karlsson. It appears that Sorour & Coney (1979) were not aware of the calculations by Roesner (1978) which had already confirmed the stabilizing effect of radial heating for the conditions of Snyder & Karlsson's experiments, at least in the infinite-aspect-ratio limit. In any event, one must bear in mind that conclusions based on a direct comparison of results between these two experiments neglect possible effects arising from the large difference in Prandtl number between water and oil.

A flow which combines both rotation and convection can be driven to instability by centrifugal, buoyancy or shear forces, acting separately or in concert. Obviously, the buoyancy-driven instability mechanism necessitates the inclusion of gravity, not only as it affects system stability but also as it determines the axial velocity field in the base flow. Numerical calculations in both infinite-aspect-ratio (Roesner 1978) and finite-aspect-ratio (Ball & Farouk 1987) systems have shown that radial heating stabilizes Taylor vortices. Roesner's stability curve is symmetric with respect to the sense of radial heating and crosses the $G = 0$ axis at zero slope. Snyder & Karlsson's stability measurements also exhibit near symmetry at small Grashof numbers, but with discontinuous slope at zero Grashof number.

## 3. Mathematical formulation and solution procedure

### 3.1. *Equations of motion and base flow*

The motion of a thermally active viscous fluid is governed by the equation of continuity, the Navier–Stokes equations and the energy equation. The Boussinesq approximation is invoked for the buoyancy term, but otherwise constant fluid properties are presumed. The equations are made dimensionless by scaling lengths with $d$, time with $d^2/\nu$, azimuthal velocity with $\Omega_1 R_1$, radial and vertical velocities with $U_0 = g\beta d^2 \Delta T/\nu$, temperature with $\Delta T = T_1 - T_2$, and the reduced pressure (thermodynamic pressure less the hydrostatic head) with $\rho_2 U_0^2$, where $\rho$ is the fluid density. Subscripts 1 and 2 denote conditions at the inner and outer cylinders located at non-dimensional radii $r_1 = \eta/(1-\eta)$ and $r_2 = 1/(1-\eta)$, respectively. The governing equations for the dimensionless velocities $(u, v, w)$, pressure $p$ and temperature $\theta$ are given by

$$\frac{\partial u}{\partial t} + G\left[u\frac{\partial u}{\partial r} + S\frac{v}{r}\frac{\partial u}{\partial \phi} + w\frac{\partial u}{\partial z} - S^2\frac{v^2}{r}\right] = -G\frac{\partial p}{\partial r} + \nabla^2 u - S\frac{2}{r^2}\frac{\partial v}{\partial \phi} - \frac{u}{r^2}, \tag{2a}$$

$$S\left[\frac{\partial v}{\partial t} + G\left(u\frac{\partial v}{\partial r} + S\frac{v}{r}\frac{\partial v}{\partial \phi} + w\frac{\partial v}{\partial z} + \frac{uv}{r}\right)\right] = -G\frac{1}{r}\frac{\partial p}{\partial \phi} + S\nabla^2 v + \frac{2}{r^2}\frac{\partial u}{\partial \phi} - S\frac{v}{r^2}, \tag{2b}$$

$$\frac{\partial w}{\partial t} + G\left[u\frac{\partial w}{\partial r} + S\frac{v}{r}\frac{\partial w}{\partial \phi} + w\frac{\partial w}{\partial z}\right] = -G\frac{\partial p}{\partial z} + \theta + \nabla^2 w, \tag{2c}$$

$$\frac{\partial \theta}{\partial t} + G\left[u\frac{\partial \theta}{\partial r} + S\frac{v}{r}\frac{\partial \theta}{\partial \phi} + w\frac{\partial \theta}{\partial z}\right] = \frac{1}{Pr}\nabla^2\theta, \tag{2d}$$

$$\frac{\partial u}{\partial r} + \frac{u}{r} + S\frac{1}{r}\frac{\partial v}{\partial \phi} + \frac{\partial w}{\partial z} = 0; \quad \nabla^2 = \frac{1}{r}\frac{\partial}{\partial r}\left(r\frac{\partial}{\partial r}\right) + \frac{1}{r^2}\frac{\partial^2}{\partial \phi^2} + \frac{\partial^2}{\partial z^2}. \tag{2e,f}$$

The dimensionless parameters $G$ and $Pr$ appearing in the equations are the previously defined Grashof and Prandtl numbers. The swirl parameter $S = \Omega_1 R_1/U_0$ appears

because of the difference in normalization between the azimuthal and meridional velocities. All computed stability results will be presented in terms of the Taylor number $Ta = 2\eta^2\Omega_1^2 d^4/\nu^2(1-\eta^2)$ in lieu of $S$. The equations describing pure natural convection with velocities normalized by the convection velocity $U_0$ are obtained by setting $S = 1$. The classical Taylor–Couette problem with velocities normalized by $\Omega_1 R_1$ is obtained by setting $S = 1$, $\theta = 0$ and replacing the Grashof number with $[Ta(1+\eta)/2(1-\eta)]^{\frac{1}{2}}$. These reductions provide a means for checking the numerical code with previously reported stability calculations in the limiting cases of pure convection and pure rotation.

The base flow solution in the conduction regime is found by assuming the motion to be steady, axisymmetric and independent of the axial coordinate. Under these conditions the equation of continuity is satisfied identically and conservation of mass is ensured by the integral constraint

$$\int_{r_1}^{r_2} r\bar{w}(r)\,\mathrm{d}r = 0, \tag{3}$$

where an overbar signifies base flow conditions. The solution of (2) satisfying (3) with boundary conditions $\bar{v} = \bar{\theta} = 1$, $\bar{w} = 0$ at $r = r_1$ and $\bar{v} = \bar{\theta} = \bar{w} = 0$ at $r = r_2$ yields

$$\bar{u}(r) = 0; \quad \bar{v}(r) = \frac{\eta}{1+\eta}\left[\frac{1}{(1-\eta)^2 r} - r\right]; \quad \bar{\theta}(r) = \frac{1}{\ln(\eta)}\ln\left(\frac{r}{r_2}\right), \tag{4a–c}$$

$$\bar{w}(r) = \frac{1}{(1-\eta)^2}\left\{\left[\frac{A}{B}\right]\left[(1-\eta)^2 r^2 - 1 + (1-\eta^2)\frac{\ln(r/r_2)}{\ln(\eta)}\right] - \frac{1}{4}[(1-\eta)^2 r^2 - \eta^2]\frac{\ln(r/r_2)}{\ln(\eta)}\right\}, \tag{4d}$$

$$\bar{p}(r) = \frac{S^2\eta^2}{(1+\eta)^2}\left\{\frac{r^2}{2} + \frac{1}{2r^2(1-\eta)^4} - \frac{1}{2(1-\eta)^2}\left(\frac{\eta^4+1}{\eta^2}\right) - \frac{2}{(1-\eta)^2}\ln\left(\frac{(1-\eta)r}{\eta}\right)\right\}, \tag{4e}$$

where $A = (1-\eta^2)(1-3\eta^2) - 4\eta^4\ln(\eta)$, and $B = 16[(1-\eta^2)^2 + (1-\eta^4)\ln(\eta)]$ are the constants in (4*d*). It may be observed that the base flow is just a superposition of the azimuthal velocity for the classical Taylor problem (Chandrasekhar 1961) and the axial velocity and temperature fields for convection in the conduction regime (Choi & Korpela 1980).

### 3.2. *Disturbance equations*

The primitive variables are written as the sum of the base flow and a perturbed flow as follows:

$$\begin{pmatrix} u \\ v \\ w \\ \theta \\ p \end{pmatrix} = \begin{pmatrix} 0 \\ \bar{v} \\ \bar{w} \\ \bar{\theta} \\ \bar{p} \end{pmatrix} + \begin{pmatrix} U(r) \\ V(r) \\ W(r) \\ \Theta(r) \\ P(r) \end{pmatrix} \exp[\mathrm{i}(Kz - n\phi + \sigma_\mathrm{i} t) + \sigma_\mathrm{r} t]. \tag{5}$$

In this formulation the disturbances are either toroidal ($n = 0$) or spiral ($n \neq 0$) with uniform axial wavenumber $K$, frequency $-\sigma_\mathrm{i}$ and growth rate $\sigma_\mathrm{r}$. The radial eigenfunctions $U(r)$, $V(r)$, $W(r)$, $\Theta(r)$ and $P(r)$ are complex quantities. Substituting (5)

into (2), subtracting the base flow (4) and neglecting higher-order terms furnishes the linear stability equations

$$\frac{\mathrm{d}^2U}{\mathrm{d}r^2} = (\sigma + \mathrm{i}KG\bar{w})\,U + G\frac{\mathrm{d}P}{\mathrm{d}r} - \frac{\mathrm{i}nSG\bar{v}}{r}U - \frac{1}{r}\frac{\mathrm{d}U}{\mathrm{d}r} + \left[K^2 + \frac{1+n^2}{r^2}\right]U - \left[\frac{2\mathrm{i}nS}{r^2} + \frac{2S^2G\bar{v}}{r}\right]V, \tag{6a}$$

$$\frac{\mathrm{d}^2V}{\mathrm{d}r^2} = (\sigma + \mathrm{i}KG\bar{w})\,V - \frac{\mathrm{i}nG}{Sr}P - \frac{\mathrm{i}nSG\bar{v}}{r}V - \frac{1}{r}\frac{\mathrm{d}V}{\mathrm{d}r} + \left[K^2 + \frac{1+n^2}{r^2}\right]V + \frac{2\mathrm{i}n}{Sr^2}U + G\left[\frac{\bar{v}}{r} + \frac{\mathrm{d}\bar{v}}{\mathrm{d}r}\right]U, \tag{6b}$$

$$\frac{\mathrm{d}^2W}{\mathrm{d}r^2} = (\sigma + \mathrm{i}KG\bar{w})\,W + G\frac{\mathrm{d}\bar{w}}{\mathrm{d}r}U + \mathrm{i}KGP - \frac{\mathrm{i}nSG\bar{v}}{r}W - \Theta - \frac{1}{r}\frac{\mathrm{d}W}{\mathrm{d}r} + \left(K^2 + \frac{n^2}{r^2}\right)W, \tag{6c}$$

$$\frac{\mathrm{d}^2\Theta}{\mathrm{d}r^2} = Pr(\sigma + \mathrm{i}KG\bar{w})\,\Theta + Pr\,G\frac{\mathrm{d}\bar{\theta}}{\mathrm{d}r}U - Pr\,\mathrm{i}nSG\frac{\bar{v}}{r}\Theta - \frac{1}{r}\frac{\mathrm{d}\Theta}{\mathrm{d}r} + \left(K^2 + \frac{n^2}{r^2}\right)\Theta, \tag{6d}$$

$$\frac{\mathrm{d}U}{\mathrm{d}r} = -\frac{U}{r} + \mathrm{i}nS\frac{V}{r} - \mathrm{i}KW. \tag{6e}$$

These equations are to be solved with homogeneous boundary conditions at $r = r_1$ and $r_2$. The phase function $(Kz - n\phi + \sigma_i t)$ in (5) with critical solution values for $n$, $K$, and $\sigma_i$ completely determines the shape and kinematics of the disturbance flow patterns at neutral stability where $\sigma_r = 0$. Specifically, the non-dimensional axial propagation speed $C$, wavelength $\lambda$ normal to lines of constant phase, and inclination $\psi$ of phase lines with respect to the horizontal are given by

$$C = \frac{-\sigma_i}{K}, \quad \lambda = \frac{2\pi}{(n^2/r^2 + K^2)^{\frac{1}{2}}}, \quad \psi = \tan^{-1}\left(\frac{n}{rK}\right). \tag{7a–c}$$

Note that the wavelength and inclination angle for the asymmetric disturbances depend on the radial coordinate; for a given mode of instability, the spiral wavelength (inclination) will be shorter (steeper) when observed at the inner wall than when observed at the outer wall.

### 3.3. *Symmetry properties of the disturbance equations*

Recalling that the dimensional temperature and axial velocity are normalized with the temperature contrast $\Delta T$, the corresponding non-dimensional variables $w$ and $\theta$ in (5) do not change sign when the sense of radial heating is reversed. A reversal of the angular velocity $\Omega_1$, on the other hand, does alter the sign of the dimensionless angular velocity $v$ in (5) even though the Taylor number remains unaffected. In the absence of rotation, equations (7) reduce to the free-convection system studied by McFadden *et al.* (1984*a*) by setting $S = 1$ and $\bar{v} = \partial\bar{v}/\partial r = 0$. In this case there exists both a degeneracy and a symmetry of the solution to the eigenvalue problem. Assume, for example, that one has a solution $[U, V, W, \Theta, P; G, K, \sigma, n]$ to the disturbance equations for natural convection satisfying homogeneous boundary conditions at the cylinder walls. The substitutions $V \to -V$ and $n \to -n$ give a new solution set $[U, (-V), W, \Theta, P; G, K, \sigma, (-n)]$ satisfying the original system of equations and boundary conditions. From (7) one finds that the orientation of the spirals is reversed and the direction of phase propagation remains the same.

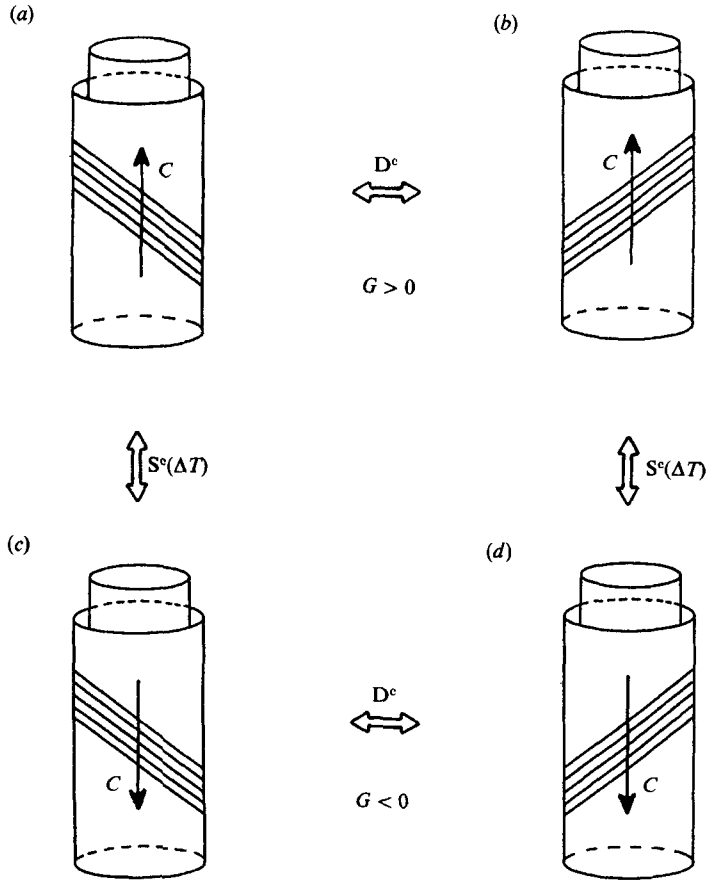


FIGURE 2. Schematic diagram of the effects of the $D^c$ degeneracy and the $S^c(\Delta T)$ heating symmetry on helical instabilities for natural convection. The spiral orientation and phase speed direction for (*a*) is that determined by numerical calculation. The remaining possibilities are a direct result of the degeneracy and symmetry.

Therefore, the two solutions comprise a degenerate solution pair and this degeneracy property is denoted $D^c$, the degeneracy for (natural) convection. Taking the complex conjugate (asterisk notation is employed) of the free-convection perturbation equations reveals a third solution set $[(-U^*), V^*, W^*, \Theta^*, P^*; (-G), K, \sigma^*, n]$. This implies that, for the same temperature contrast $|\Delta T|$, every solution for a heated inner wall has a corresponding solution for a heated outer wall. According to (7) the only distinguishing feature between these two solutions is the reversed direction of axial phase propagation. We denote this symmetry property as $S^c(\Delta T)$, the symmetry with respect to radial heating for (natural) convection. Formally, we have proven the following results:

$D^c$ degeneracy

If $[U, V, W, \Theta, P; G, K, \sigma, n]$ is a solution of the linearized disturbance equations describing the stability of natural convection in a differentially heated vertical annulus of infinite aspect ratio, then $[U, (-V), W, \Theta, P; G, K, \sigma, (-n)]$ is also a solution.

$S^c(\Delta T)$ symmetry†
If $[U, V, W, \Theta, P; G, K, \sigma, n]$ is a solution of the linearized disturbance equations describing the stability of natural convection in a differentially heated vertical annulus of infinite aspect ratio, then $[(-U^*), V^*, W^*, \Theta^*, P^*; (-G), K, \sigma^*, n]$ is also a solution.

Manifestations of the $D^c$ degeneracy and the $S^c(\Delta T)$ symmetry are sketched in figure 2 for appropriate combinations of $(C, \psi)$ determined from critical solutions for $(\sigma_i, n)$ reported in §4.2. By definition, $G > 0$ implies a relatively hot inner wall. Note that forward or reverse application of $D^c$ followed by $S^c(\Delta T)$ furnishes a fourth solution set $[(-U^*), (-V^*), W^*, \Theta^*, P^*; (-G), K, \sigma^*, (-n)]$, the disturbance waveform characteristics of which are depicted in figure 2(d).

For Taylor–Couette flow with radial heating two symmetries are found. Suppose one has a solution $[U, V, W, \Theta, P; Ta, G, K, \sigma, n]$ of the full disturbance equations (6) satisfying homogeneous boundary conditions. The substitutions $\Omega_1 \rightarrow -\Omega_1$ and $n \rightarrow -n$ yield another solution for which the orientation of the spirals is reversed but the phase speed remains the same. This solution pair is denoted $S^{c/r}(\Omega)$, the symmetry with respect to rotation for flow in the convecting/rotating system. Thus non-zero rotation of the inner cylinder breaks the $D^c$ degeneracy for free convection. Taking the complex conjugate of (6) one can identify a third solution for which both spiral inclination and axial phase speed are reversed. This symmetry property is denoted $S^{c/r}(\Delta T)$, the symmetry with respect to radial heating for flow in the convecting/rotating system. Formally, these symmetries for radially heated Taylor–Couette flow may be written as follows:

$S^{c/r}(\Omega)$ symmetry
If $[U, V, W, \Theta, P; Ta, G, K, \sigma, n]$ comprises a solution of the linearized disturbance equations describing the stability of flow in a differentially heated vertical annulus of infinite aspect ratio with inner cylinder rotating, then $[U, (-V), W, \Theta, P; Ta, G, K, \sigma, (-n)]$ is the solution when the inner cylinder counter-rotates at the same speed.

$S^{c/r}(\Delta T)$ symmetry
If $[U, V, W, \Theta, P; Ta, G, K, \sigma, n]$ comprises a solution of the linearized disturbance equations describing the stability of flow in a differentially heated vertical annulus of infinite aspect ratio with inner cylinder rotating, then $[(-U^*), V^*, W^*, \Theta^*, P^*; Ta, (-G), K, \sigma^*, (-n)]$ is also a solution for the same rotation of the inner cylinder.

The effects of the $S^{c/r}(\Omega)$ and $S^{c/r}(\Delta T)$ symmetries are depicted in figure 3 for appropriate combinations of $(C, \psi)$ determined by numerical solution. Forward or reverse application of the two symmetry operations yields the fourth solution set $[(-U^*), (-V^*), W^*, \Theta^*, P^*; Ta, (-G), K, \sigma^*, n]$ with spiral wave characteristics as sketched in figure 3(*d*). Note that the $S^{c/r}(\Delta T)$ symmetry provides a formal proof for the symmetric stability boundary calculated by Rosener (1978) for axisymmetric disturbances and ensures this symmetry for all asymmetric modes as well.

† This result was discovered through numerical computation and subsequently verified by a tedious study of the sixteen first-order ordinary differential equations describing linearized stability (Ali 1988). The more elegant proof given here is due to Dr Geoffrey McFadden of the National Institute of Standards and Technology, Gaithersburg, PA.

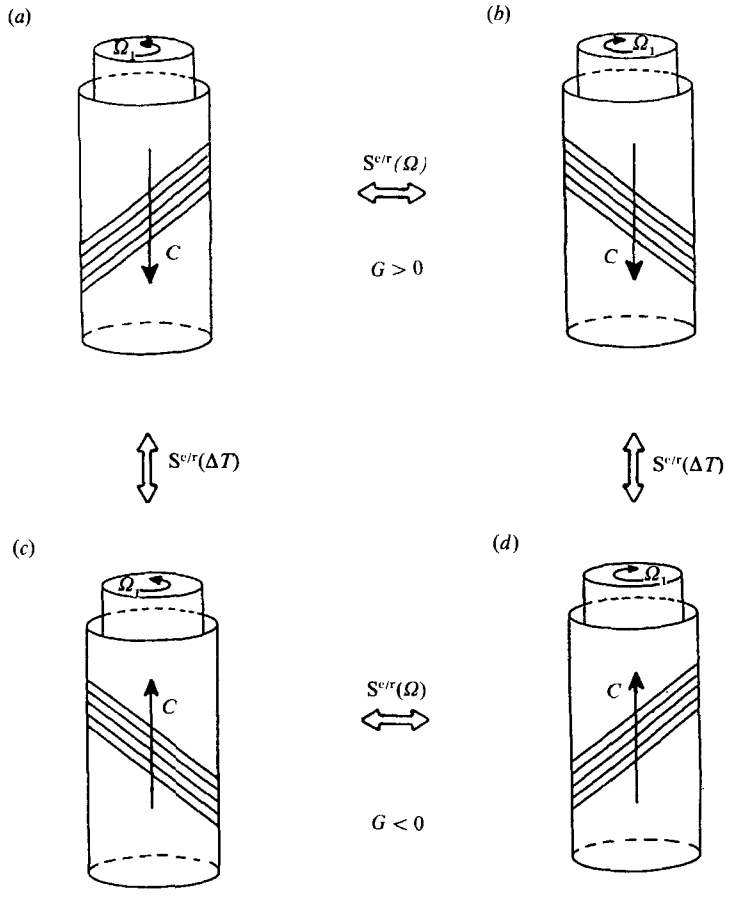


FIGURE 3. Schematic diagram of the effects of the $S^{e/r}(\Omega)$ rotation symmetry and the $S^{e/r}(\Delta T)$ heating symmetry on helical instabilities for circular Couette flow with radial heating. The spiral orientation and phase speed direction for (*a*) is that determined by numerical calculation. The remaining possibilities are a direct result of the two symmetries.

### 3.4. *Numerical solution procedure*

The usual method of eliminating the pressure by cross-differentiation and reducing the system to a set of first-order equations for the real and imaginary components of the primitive variables is extremely tedious. It is far simpler to follow Garg & Rouleau (1972) and Garg (1981) and introduce new complex velocities $f(r)$ and $g(r)$ defined by

$$f(r) = U(r) + \mathrm{i}V(r), \quad g(r) = U(r) - \mathrm{i}V(r). \tag{8a, b}$$

It is then fairly straightforward to derive the set of sixteen real first-order ordinary differential equations describing linear stability. For these the interested reader is referred to Ali (1988). The system is solved subject to homogeneous boundary conditions at $r = r_1$ and $r_2$ using the linear boundary-value problem software package SUPORT (Scott & Watts 1977) in combination with the nonlinear equation solver SNSQE (SLATEC; Powell 1970). To avoid singular matricies, the procedure described by Keller (1976) is followed wherein one of the complex boundary conditions, say $W = 0$ at $r = r_2$, is replaced by the boundary condition $\mathrm{d}W/\mathrm{d}r = 1$ at $r = r_2$. For given

values of the parameters, a solution of the linear system can be determined which generally will not satisfy $W = 0$ at $r = r_2$. The two parameters chosen to be eigenvalues are then varied until both the real and imaginary parts of $W(r)$ are driven to zero at the outer boundary. The object of this study is to determine curves of neutral stability for which $\sigma_r = 0$. Hence the eigenvalue problem may be written symbolically as

$$F(G, Ta, Pr, K, \sigma_i, n, \eta) = 0. \tag{9}$$

The parameters $Ta$, $Pr$, $K$, $n$ and $\eta$ are usually fixed and solution of the ordinary differential equations is obtained by iteration on the eigenvalue pair $(G, \sigma_i)$. At fixed mode number a search is conducted to find the minimum Grashof number over all wavenumbers $K$, denoted here by $G_n$. Critical conditions are then determined as the minimum $G_n$ over all positive and negative values of $n$, and the critical values so obtained are denoted $G_c$, $Ta_c$, $K_c$ and $(\sigma_i)_c$. In some instances solutions were more readily obtained by fixing $G$, $Pr$, $K$, $n$ and $\eta$, and iterating on the eigenvalue pair $(Ta, \sigma_i)$. Minimum values for either $G_c$ or $Ta_c$ were determined by incrementing the wavenumber in steps $\Delta K = 0.01$. The relative error incurred in the stepping procedure depends on the shape of the neutral stability curve in the vicinity of the minimum as well as its magnitude. An analysis of results shows that relative errors for the reported values of $G_c$ and $Ta_c$ are on the order of 0.05% with a worst case of about 0.2%. Computations were performed in double precision on a Pyramid 90X or in single precision on a Cyber 205.

### 3.5. *Parameter selection and code testing*

Owing to the large number of parameters governing this problem, we limit the investigation primarily to three Prandtl numbers, $Pr = 4.35$, 15 and 100, and two radius ratios, $\eta = 0.60$ and 0.959. The combination $Pr = 4.35$ at $\eta = 0.959$ corresponds to the reported conditions for Snyder & Karlsson's (1964) narrow-gap experiments in water, and this radius ratio is also considered at $Pr = 100$ to investigate the effect of fluid properties on the narrow-gap geometry. The combinations $Pr = 15$ and $Pr = 100$ at $\eta = 0.6$ provide wide-gap examples corresponding to cases studied by Choi & Korpela (1980) in the pure-convection limit. The case $Pr = 15$ was selected because both buoyancy and shear forces are known to be in direct competition for triggering instability. The results of McFadden *et al.* (1984*a*) show that for the parameters of this investigation computed stability boundaries must evolve from axisymmetric Taylor cells at $G = 0$ to axisymmetric shear-driven or buoyancy-driven instabilities at $Ta = 0$.

The numerical code was tested by computing conditions for critical stability in the limiting cases of zero differential heating and zero cylinder rotation. A calculation of minimum Taylor numbers $Ta_n$ for mode numbers $0 \leqslant n \leqslant 4$ at selected radius ratios in the range $0.6 \leqslant \eta \leqslant 0.95$ compared to within 0.01% with results published by Sparrow, Munro & Jonsson (1964), Walowit *et al.* (1964) and Roberts (1965). To compare with published results in the natural-convection limit, critical Grashof numbers $(G_c)_0 \equiv G_c(\Omega = 0)$ were computed at selected radius ratios and Prandtl numbers in the ranges $0.1 \leqslant \eta \leqslant 0.6$ and $0 \leqslant Pr \leqslant 100$ for $n = 0$ and 1. The results reported by McFadden *et al.* (1984*a*) were reproduced within 0.01%, and generally 1% agreement with the Galerkin calculations of Choi & Korpela (1980) was obtained. Also, guided by the latter investigation, entire neutral stability curves at $Pr = 4.35$, 15 and 100 for modes $n = 0$ and 1 were generated in order to gain experience in locating new stability branches. This exercise proved invaluable because, although

the present solution procedure is more accurate than the Galerkin method, it has the disadvantage that a good initial guess for the eigenvalue pair is necessary to ensure convergence.

## 4. Presentation of results

Some general comments with respect to the overall results are given here. First, all critical conditions were found in the range $0.15 < K_c < 4.0$ and these $O(1)$ values verify that the gap width $d$ is the correct scale for the wavelength of the unstable modes. Second, by virtue of the $S^c(\Delta T)$ and $S^{c/r}(\Delta T)$ symmetries, the present computations were carried out only for $G \geqslant 0$. Third, the critical spiral modes for $G > 0$ were always associated with positive values of $n$ and $\sigma_i$, corresponding to positive spiral inclination and downward axial phase speed as sketched in figure 3(*a*). Finally, not all the spiral modes for the narrow gap were located. As will become evident, the number of competing critical modes increases with increasing radius ratio. At $\eta = 0.6$ there were sufficiently few modes that the entire $Ta_c$–$G$ stability diagram at the three fixed Prandtl numbers could be completely determined with reasonable effort. For $\eta = 0.959$, however, as many as 55 critical modes were discovered. It was felt that the understanding gained by locating all the mode branches was not worth the intensive effort necessary to complete the task. Therefore, for the narrow gap only the first ten or so asymmetric modes were followed, the terminal spiral mode was located, and the nature of stability results for the intervening modes is inferred by interpolation.

### 4.1. *Neutral stability curves*

In the process of locating critical stability boundaries, neutral stability curves of $Ta$ versus $K$ or $G$ versus $K$ were generated for given values of $Pr$, $\eta$ and $n$. We note a persistent feature observed during this search. Computations revealed that the usual parabolic open-loop $Ta$–$K$ neutral stability curves were often accompanied by a set of closed-loop branches in a limited range of overlapping values of $G$ as shown in figure 4 for $Pr = 15$ and $n = 2$. The closed-loop neutral curve in figure 4(*a*) is seen in figure 4(*b*) to encompass smaller loops that degenerate to a point at $G = 254$ where $Ta = 217$ and $K = 2.33$. Beyond this limiting point we were not able follow solutions in $Ta$–$K$ space but did locate them in $G$–$K$ space by switching the eigenvalue pair from $(Ta, \sigma_i)$ to $(G, \sigma_i)$. The limit points were found to be associated with a turning point of the $Ta$–$G$ stability curve as shown in figure 5 for a different case with $Pr = 100$ and $n = 2$. As depicted by the inset drawings, the lower branch of the stability boundary is formed from minimum values of $Ta_n$ on the closed loops, while the upper branch is formed from minimum values of $G_n$ on the open loops. A curve fit to the stability boundary in figure 5 gives a turning-point value $G \approx 50.3$, virtually identical to that estimated for the degenerate point of the closed loops. This feature is a manifestation of the complicated three-dimensional topology of the stability curves in $Ta$–$G$–$K$ space. Similar closed-loop stability maps have been reported by Hart (1971) for convection in an inclined heated box and by McFadden *et al.* (1984*b*) in a study of the stability of crystal morphology driven by fluid flow in the melt. In the present calculations we were able to continue tracking the stability diagram beyond the degenerate point of the closed-loop stability curves by a change in the eigenvalue pair.

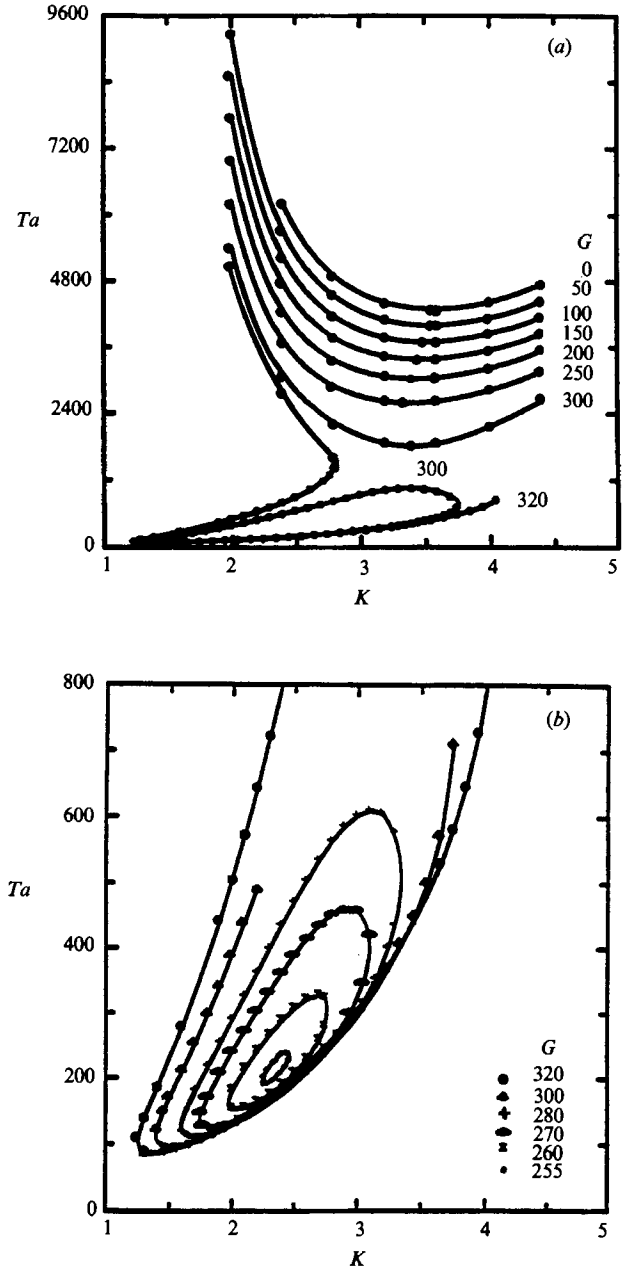


FIGURE 4. Neutral stability curves for mode 2 at $Pr = 15$ and $\eta = 0.6$. (*a*) Diagram showing simultaneous occurrence of open- and closed-loop branches at $G = 300$; (*b*) enlarged view of the closed-loop neutral curves showing the evolution to their point of degeneracy at $G \approx 254$ where $Ta \approx 217$ and $K \approx 2.33$.

### 4.2. *Critical stability results*

Sample computed critical Taylor numbers, Grashof numbers, mode numbers, wavenumbers and phase speeds for the $(Pr, \eta)$ combinations (4.35, 0.6), (15, 0.6), (100, 0.6), (4.35, 0.959) and (100, 0.959) are listed in tables 1 (*a*)–1 (*e*), respectively. The log-log stability diagram in figure 6 clearly exhibits the destabilizing effect of Prandtl

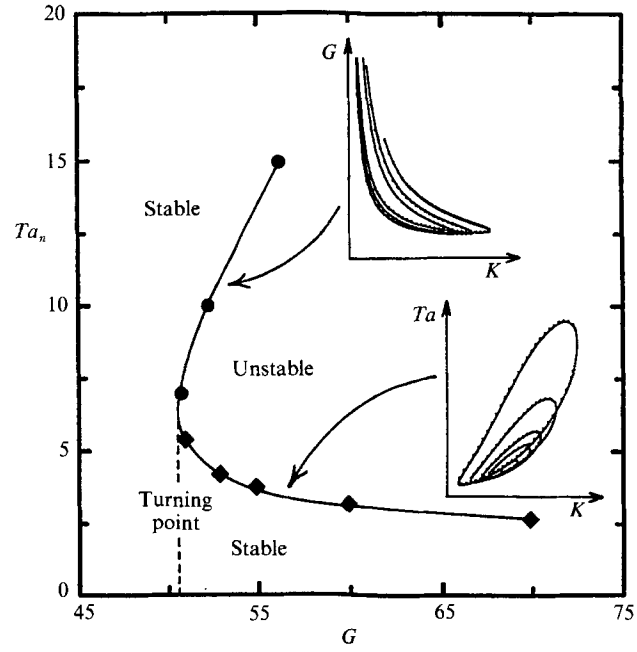


FIGURE 5. Illustration of the turning point for mode 2 instability at $Pr = 100$ and $\eta = 0.6$. The turning point at $G \approx 50.3$ corresponds to the limit point for the closed-loop neutral stability curves shown in the lower inset. Minima from the closed $Ta$–$K$ loops and the open $G$–$K$ loops contribute critical points to the stability diagram below and above the turning point, respectively.

number for the wide-gap geometry. Each stability boundary emanates from the same critical isothermal Taylor number $(Ta_c)_0 = 2572$ calculated for $\eta = 0.6$. The critical curves progressively lose stability to spiral modes $n = 1$, 2, 3 and 4 with increased radial heating. Observe that each fourth spiral mode branch intersects its Prandtl-number-dependent axisymmetric convection mode branch in a virtually perpendicular manner. These branches are then followed at nearly constant Grashof number to the critical terminal values $(G_c)_0 = 8354$, 2209 and 644 corresponding to $Pr = 4.35$, 15 and 100, respectively. It can be inferred from the results of Choi & Korpela (1980) that for $Pr = 4.35$ instability evolves from centrifugally driven to shear driven as the stability boundary is traversed from low to high Grashof number, while for $Pr = 100$ it evolves from centrifugally driven to buoyancy driven. For $Pr = 15$ the evolution is from a centrifugal instability at low Grashof number to one where buoyancy and shear forces compete at a similar level to trigger instability at high Grashof number on the axisymmetric convection branch. Note also that the turning-point behaviour discussed in §4.1 gives rise to local double-valued solutions along the critical stability boundary for the $n = 2$ spiral mode at $Pr = 15$ and for both the $n = 1$ and $n = 2$ modes at $Pr = 100$. Moreover, this multiple-valued behaviour is evident on a much larger scale for $Pr = 100$. For example, if in an experiment one were to increase cylinder rotation from rest along a line of constant Grashof number in the neighbourhood $G \approx 100$, instability to the fourth spiral mode at low Taylor number would be encountered first. At a much elevated Taylor number the flow would experience restabilization and this in turn would be followed at yet higher Taylor number by a second transition to an axisymmetric instability.

The stability boundaries for $\eta = 0.959$ given in figure 7 also exhibit strong Prandtl-

| | $n$ | $Ta_c$ | $G_c$ | $K_c$ | $(\sigma_i)_c$ |
|---|---|---|---|---|---|
| (*a*) | 0 | 0.2572 (+04) | 0.0000 (+00) | 0.3130 (+01) | 0.0000 (+00) |
| | 0 | 0.2573 (+04) | 0.1500 (+02) | 0.3150 (+01) | −0.1484 (+00) |
| | 0 | 0.2591 (+04) | 0.5000 (+02) | 0.3150 (+01) | −0.5029 (+00) |
| | 0 | 0.2611 (+04) | 0.7200 (+02) | 0.3150 (+01) | −0.7376 (+00) |
| | 1 | 0.1771 (+04) | 0.3000 (+03) | 0.2570 (+01) | 0.1296 (+02) |
| | 2 | 0.9084 (+03) | 0.5000 (+03) | 0.2340 (+01) | 0.1879 (+02) |
| | 3 | 0.3803 (+03) | 0.7000 (+03) | 0.1880 (+01) | 0.1867 (+02) |
| | 4 | 0.1283 (+03) | 0.3000 (+04) | 0.4500 (+00) | 0.1611 (+02) |
| | 0 | 0.1224 (+03) | 0.8324 (+04) | 0.2730 (+01) | −0.3549 (+02) |
| | 0 | 0.0000 (+00) | 0.8354 (+04) | 0.2750 (+01) | −0.3572 (+02) |
| (*b*) | 0 | 0.2572 (+04) | 0.0000 (+00) | 0.3130 (+01) | 0.0000 (+00) |
| | 0 | 0.2595 (+04) | 0.5000 (+02) | 0.3110 (+01) | −0.1486 (+01) |
| | 0 | 0.2586 (+04) | 0.5500 (+02) | 0.3100 (+01) | −0.1650 (+01) |
| | 1 | 0.1763 (+04) | 0.1500 (+03) | 0.3110 (+01) | 0.1316 (+02) |
| | 2 | 0.1111 (+03) | 0.2800 (+03) | 0.1680 (+01) | 0.6589 (+01) |
| | 3 | 0.6130 (+02) | 0.3200 (+03) | 0.1690 (+01) | 0.7532 (+01) |
| | 4 | 0.2688 (+02) | 0.7000 (+03) | 0.7700 (+00) | 0.7200 (+01) |
| | 0 | 0.2373 (+02) | 0.2202 (+04) | 0.1900 (+01) | −0.3600 (+02) |
| | 0 | 0.0000 (+00) | 0.2209 (+04) | 0.1850 (+01) | −0.3526 (+02) |
| (*c*) | 0 | 0.2572 (+04) | 0.0000 (+00) | 0.3150 (+01) | 0.0000 (+00) |
| | 0 | 0.2000 (+04) | 0.5481 (+02) | 0.3050 (+01) | −0.2021 (+01) |
| | 0 | 0.1800 (+04) | 0.8150 (+02) | 0.3020 (+01) | −0.2724 (+01) |
| | 0 | 0.1550 (+04) | 0.1225 (+03) | 0.3000 (+01) | −0.3787 (+01) |
| | 1 | 0.1000 (+03) | 0.6037 (+02) | 0.3200 (+01) | 0.2960 (+01) |
| | 2 | 0.4129 (+01) | 0.5300 (+02) | 0.1710 (+01) | 0.1265 (+01) |
| | 3 | 0.1631 (+01) | 0.7000 (+02) | 0.1300 (+01) | 0.1259 (+01) |
| | 4 | 0.9183 (+00) | 0.2000 (+03) | 0.4900 (+00) | 0.1344 (+01) |
| | 0 | 0.2000 (+01) | 0.6422 (+03) | 0.2500 (+01) | −0.1480 (+02) |
| | 0 | 0.0000 (+00) | 0.6436 (+03) | 0.2600 (+01) | −0.1537 (+02) |
| (*d*) | 0 | 0.1744 (+04) | 0.0000 (+00) | 0.3150 (+01) | 0.0000 (+00) |
| | 1 | 0.1736 (+04) | 0.2500 (+02) | 0.3120 (+01) | 0.3526 (+01) |
| | 2 | 0.1717 (+04) | 0.5000 (+02) | 0.3100 (+01) | 0.8751 (+01) |
| | 3 | 0.1643 (+04) | 0.1300 (+03) | 0.3010 (+01) | 0.1265 (+02) |
| | 4 | 0.1563 (+04) | 0.2000 (+03) | 0.2950 (+01) | 0.1635 (+02) |
| | 5 | 0.1495 (+04) | 0.2500 (+03) | 0.2890 (+01) | 0.1996 (+02) |
| | 6 | 0.1393 (+04) | 0.3300 (+03) | 0.2800 (+01) | 0.2301 (+02) |
| | 7 | 0.1274 (+04) | 0.4200 (+03) | 0.2700 (+01) | 0.2558 (+02) |
| | 8 | 0.1193 (+04) | 0.4750 (+03) | 0.2670 (+01) | 0.2826 (+02) |
| | 9 | 0.9558 (+03) | 0.7000 (+03) | 0.2100 (+01) | 0.2814 (+02) |
| | 52 | 0.6444 (+02) | 0.7850 (+04) | 0.3300 (+00) | 0.4269 (+02) |
| | 0 | 0.0000 (+00) | 0.7865 (+04) | 0.2750 (+01) | −0.2830 (+01) |
| (*e*) | 0 | 0.1744 (+04) | 0.0000 (+00) | 0.3150 (+01) | 0.0000 (+00) |
| | 1 | 0.2816 (+03) | 0.4000 (+02) | 0.3150 (+01) | 0.2489 (+01) |
| | 2 | 0.1200 (+03) | 0.4426 (+02) | 0.2500 (+01) | 0.2218 (+01) |
| | 3 | 0.2384 (+02) | 0.5000 (+02) | 0.1600 (+01) | 0.1482 (+01) |
| | 4 | 0.2500 (+02) | 0.4560 (+02) | 0.2250 (+01) | 0.2024 (+01) |
| | 5 | 0.1255 (+02) | 0.4600 (+02) | 0.2000 (+01) | 0.1793 (+01) |
| | 6 | 0.1000 (+02) | 0.4591 (+02) | 0.2150 (+01) | 0.1921 (+01) |
| | 7 | 0.5000 (+01) | 0.4857 (+02) | 0.1700 (+01) | 0.1585 (+01) |
| | 8 | 0.5000 (+01) | 0.4665 (+02) | 0.1950 (+01) | 0.1811 (+01) |
| | 9 | 0.3000 (+01) | 0.4919 (+02) | 0.1690 (+01) | 0.1579 (+01) |
| | 10 | 0.3000 (+01) | 0.4723 (+02) | 0.1950 (+01) | 0.1754 (+01) |
| | 11 | 0.3000 (+01) | 0.4683 (+02) | 0.2140 (+01) | 0.1929 (+01) |
| | 12 | 0.1141 (+01) | 0.5500 (+02) | 0.1400 (+01) | 0.1445 (+01) |
| | 55 | 0.1201 (+00) | 0.6000 (+03) | 0.1900 (+00) | 0.1948 (+01) |
| | 0 | 0.0000 (+00) | 0.7375 (+03) | 0.2450 (+01) | −0.1492 (+02) |

TABLE 1. Sample calculations of critical Taylor numbers $Ta_c$, Grashof numbers $G_c$, wavenumbers $K_c$ and frequencies $(-\sigma_i)_c$ at each mode number $n$ for (*a*) $\eta = 0.6$ and $Pr = 4.35$. (*b*) $\eta = 0.6$ and $Pr = 15$; (*c*) $\eta = 0.6$ and $Pr = 100$; (*d*) $\eta = 0.959$ and $Pr = 4.35$; (*e*) $\eta = 0.959$ and $Pr = 100$.

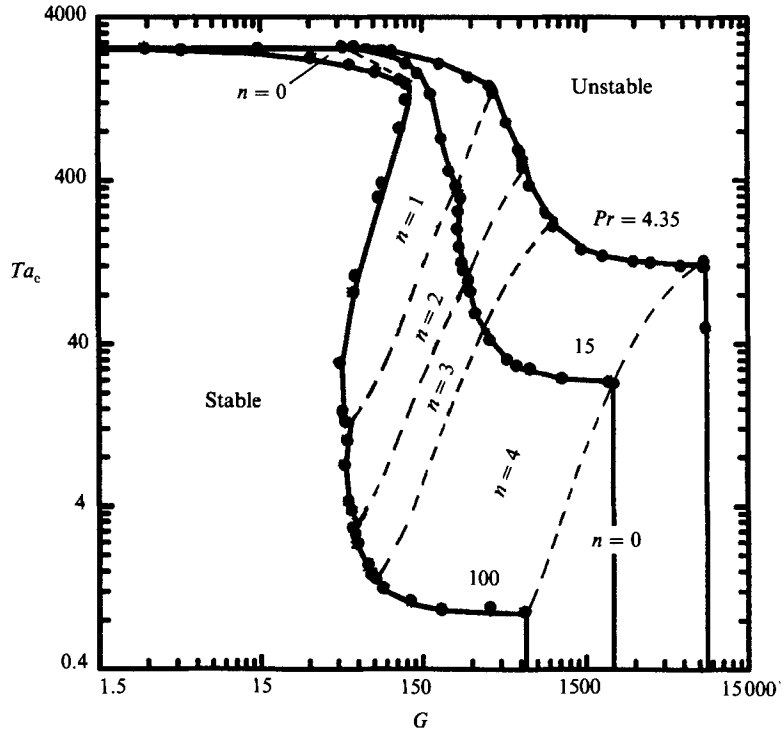


FIGURE 6. Prandtl-number variation of the critical stability boundaries for the wide-gap geometry at $\eta = 0.6$.

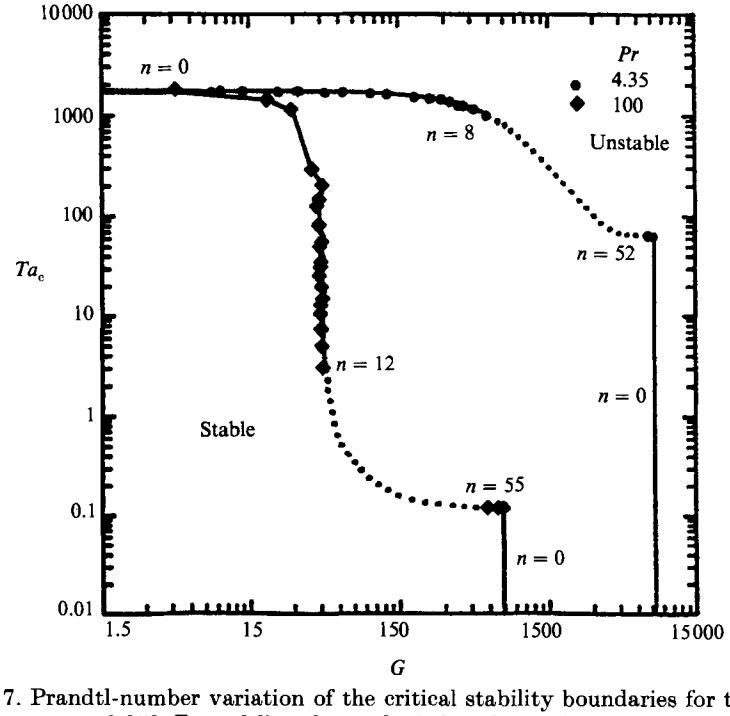


FIGURE 7. Prandtl-number variation of the critical stability boundaries for the narrow-gap geometry at $\eta = 0.959$. Dotted line shows the inferred contribution of the missing modes.

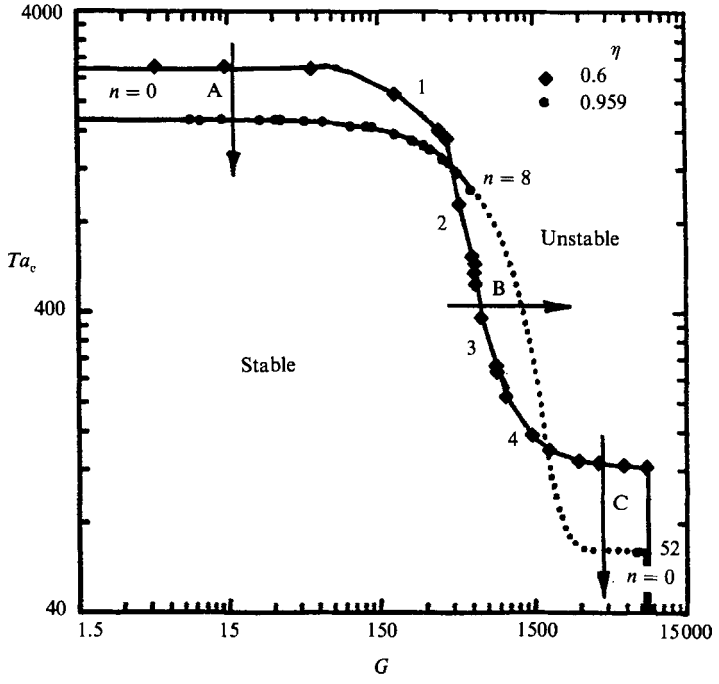


FIGURE 8. Radius-ratio variation of the critical stability boundaries for $Pr = 4.34$. Arrows indicate the direction of increasing $\eta$. Dotted line shows the inferred contribution of the missing modes for $\eta = 0.959$.

number stabilization. Here the critical curves originate from $(Ta_c)_0 = 1744$, bifurcate across more than 50 spiral modes to intersect the natural-convection branches which are then followed to their terminal values $(G_c)_0 = 7865$ and 737.5 corresponding to $Pr = 4.35$ and 100, respectively. We have located only the first eight modes for $Pr = 4.35$ and the first 12 modes for $Pr = 100$. A search along the convection branches shows that the spiral modes terminate at $n = 52$ for $Pr = 4.35$ and $n = 55$ for $Pr = 100$. As in figure 6, the terminating spiral modes make an approximately perpendicular intersection with their respective convection branches and this information has been used to sketch the interpolated stability boundary (dotted curves) for the missing spiral modes in figure 7. The successively smaller contributions from the higher mode numbers in the log-log presentation and the short sections corresponding to the terminal spiral modes suggest that all intermediate modes will be present in ordered sequence along the critical stability boundaries. Ali (1988) has shown that a partial collapse of the Prandtl-number-dependent stability boundaries in figures 6 and 7 may be obtained by plotting $Ta_c$ against Rayleigh number instead of Grashof number. Figure 8 shows the effect of radius ratio at $Pr = 4.35$ with directions of increasing $\eta$ indicated by the arrows. Increasing the radius ratio produces destabilization in regions A and C and stabilization in the intermediate region B. Similar results are found for $Pr = 100$.

The evolution of critical axial phase speeds, disturbance wavelengths and spiral inclination angles along the stability boundary are given in figures 9, 10 and 11, respectively. These figures compare wide- and narrow-gap results at $Pr = 4.35$. The values for $\lambda_c$ and $\psi_c$ were computed from equations (7*b*, *c*) at a radial position very near the outer cylindrical wall. Thus the spiral wavelengths and inclination angles

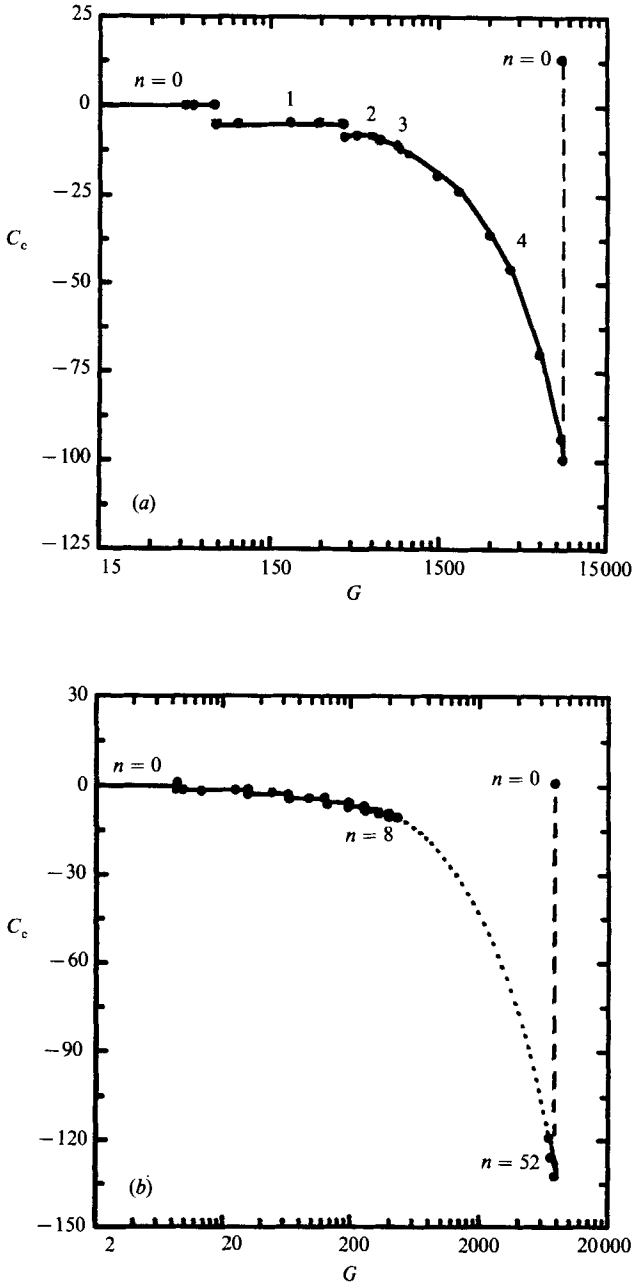


FIGURE 9. A comparison of the evolution of vertical phase propagation speeds across (*a*) the four spiral modes for $\eta = 0.6$ and (*b*) the 52 spiral modes for $\eta = 0.959$ at $Pr = 4.35$. The dotted line shows the inferred contribution of the missing modes for $\eta = 0.959$.

are indicative of what one would observe from outside a transparent annulus using particle suspensions to visualize the flow (cf. Weidman 1989) in a laboratory experiment. In these figures the interpolated contributions from missing spiral modes are indicated by the dotted lines. The axial phase speeds presented in figure 9 show that radial heating imparts a slight upward drift to the Taylor cells, but bifurcation

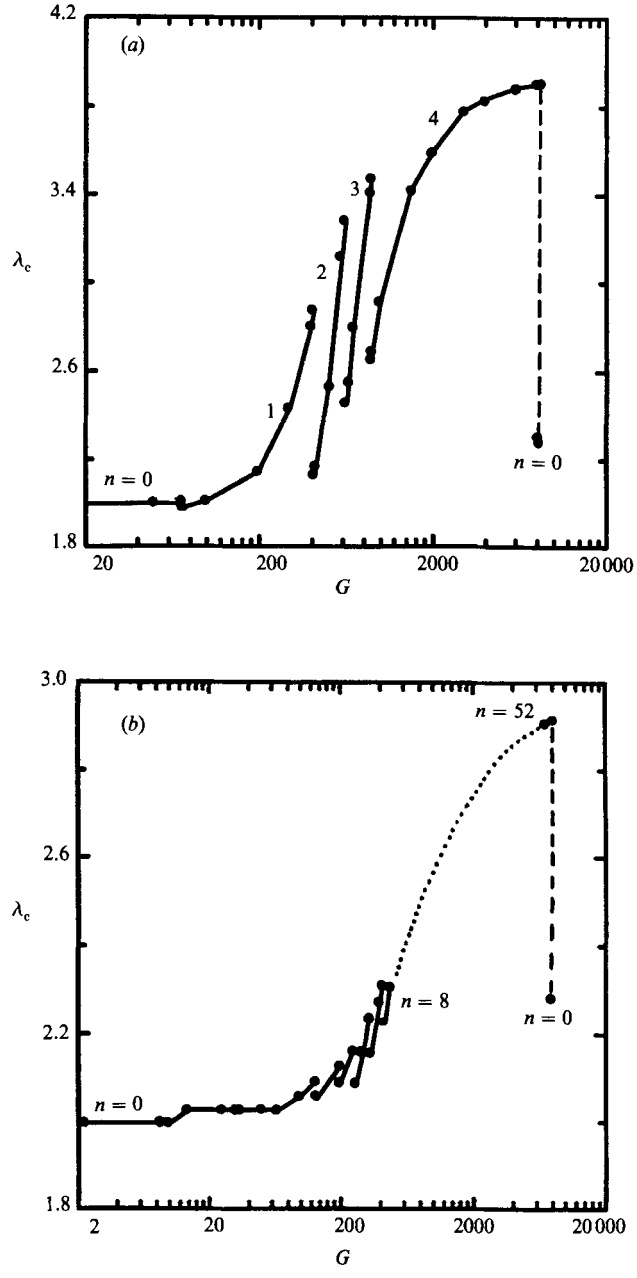


FIGURE 10. A comparison of the evolution of wavelengths normal to the phase lines across (*a*) the four spiral modes for $\eta = 0.6$ and (*b*) the 52 spiral modes for $\eta = 0.959$ at $Pr = 4.35$. The dotted line shows the inferred contribution of the missing modes for $\eta = 0.959$.

to the spiral modes at higher Grashof number induces successively stronger downward axial propagation speeds with weak discontinuities across each transition. The final transition to natural convection leaves each system in a state of slow upward drift of toroidal cells. Maximum axial phase speeds for the terminal spiral modes on the order of $C_c \approx -100$ are observed for both wide and narrow gaps. Instability wavelengths presented in figure 10 increase from $\lambda_c \approx 2.0$ for isothermal

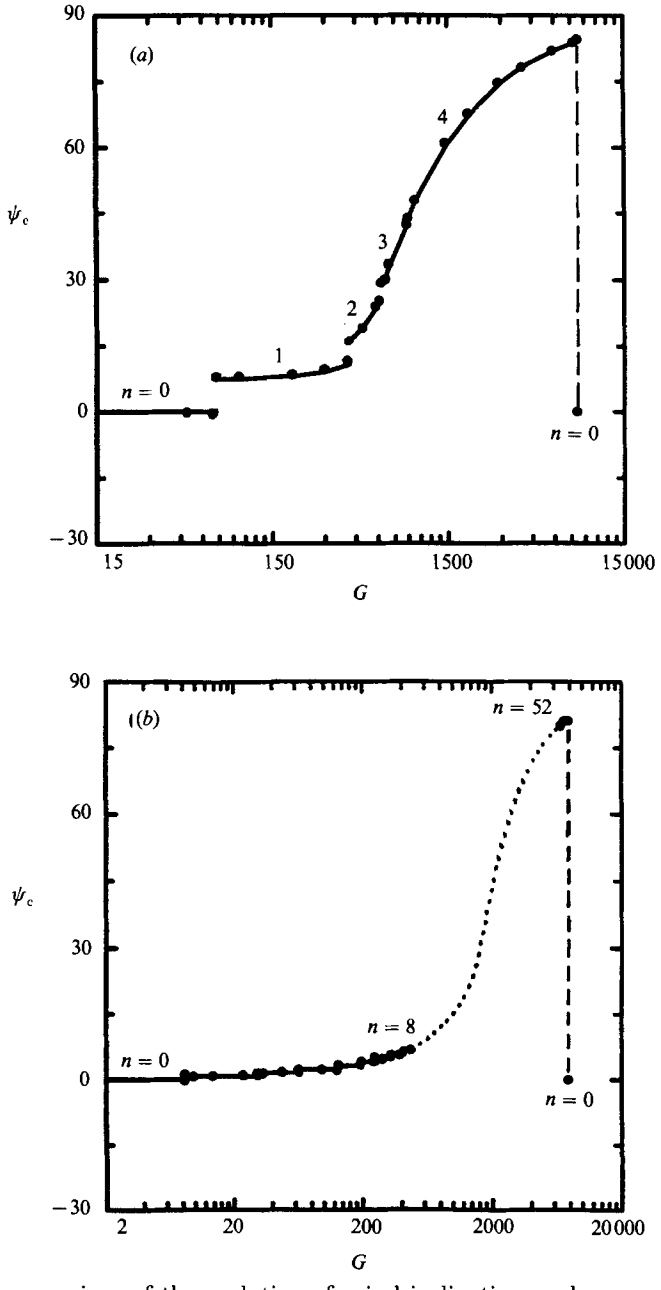


FIGURE 11. A comparison of the evolution of spiral inclination angles across (*a*) the four spiral modes for $\eta = 0.6$ and (*b*) the 52 spiral modes for $\eta = 0.959$ at $Pr = 4.35$. The dotted line shows the inferred contribution of the missing modes for $\eta = 0.959$.

and weakly heated Taylor cells across the spiral modes to maximum values $\lambda_c \approx 3.9$ for $\eta = 0.6$ and $\lambda_c \approx 2.9$ for $\eta = 0.959$. One observes, particularly for the wide gap in figure 10(a), that the wavelengths of successive helical modes grow continuously and then suddenly shrink to admit a new counter-rotating cell pair into the annulus. It is interesting to note that the wavelength of the terminal free-convection mode is only slightly larger than the wavelength of the initial Taylor vortex mode in both the

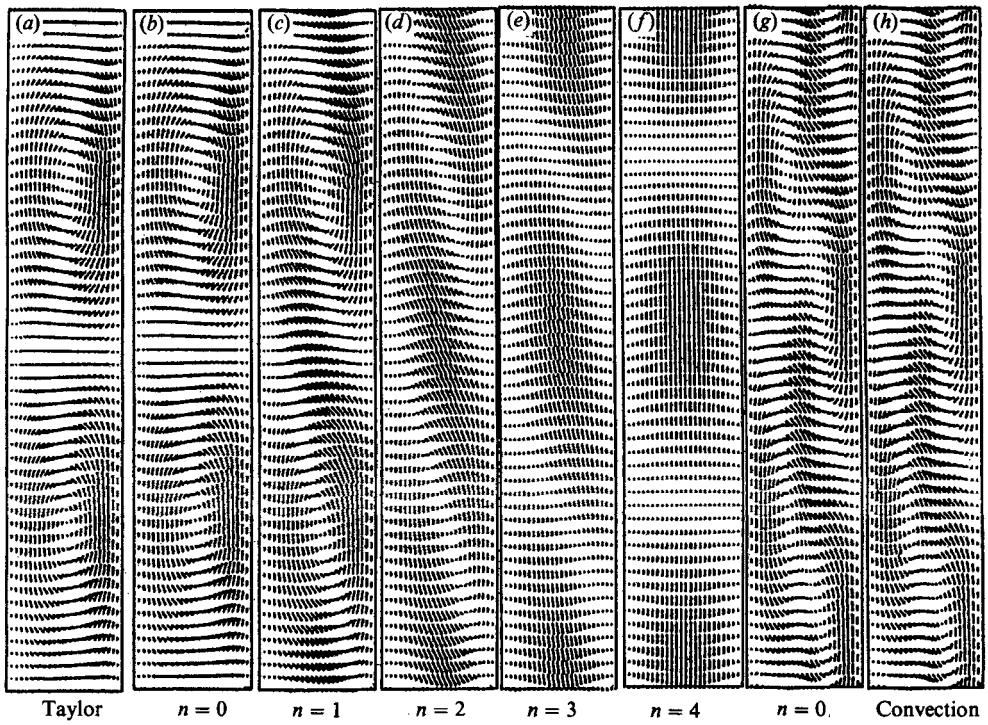


FIGURE 12. Evolution of the disturbance velocity vector fields in a meridional section at instability for $\eta = 0.6$ and $Pr = 4.35$. The left wall of each figure locates the outer cylinder. Vertical wavelengths have been scaled to equal height. The actual wavelengths can be computed from the critical conditions: (*a*) $Ta_c = 2572$, $G_c = 0$, $K_c = 0.313$; (*b*) $Ta_c = 2573$, $G_c = 15$, $K_c = 3.15$; (*c*) $Ta_c = 2109$, $G_c = 200$, $K_c = 2.90$; (*d*) $Ta_c = 908$, $G_c = 500$, $K_c = 2.34$; (*e*) $Ta_c = 380$, $G_c = 700$, $K_c = 1.88$; (*f*) $Ta_c = 123$, $G_c = 8000$, $K_c = 0.17$; (*g*) $Ta_c = 50$, $G_c = 8325$, $K_c = 2.75$; (*h*) $Ta_c = 0$, $G_c = 8354$, $K_c = 2.75$.

wide- and narrow-gap configurations. Figure 11 shows the evolution of spiral inclination angle. At both values of $\eta$ the heated horizontal Taylor cells give way to spirals which tilt successively upward with the admission of each new helical wave. Note that the terminal spiral modes become nearly vertical just before the final abrupt transition to horizontal convection cells.

Plotted results for $C_c, \lambda_c$ and $\psi_c$ showing the influence of Prandtl number for the wide gap at $\eta = 0.6$ are given in Weidman & Ali (1989). Apart from the $n = 1$ mode branches, which exhibit curious multiple-valued behaviour, the evolution of these quantities at $Pr = 100$ is qualitatively the same as those displayed in figures 9(*a*), 10(*a*) and 11(*a*) for $Pr = 4.35$. That is, the cells of a given spiral mode gradually expand and then suddenly contract when a new wave is admitted, and the spirals tilt continuously upward becoming nearly vertical in the fourth spiral mode. The only fundamental difference is that the axial phase speeds for the spiral waves at $Pr = 100$ are an order of magnitude smaller than their counterparts at $Pr = 4.35$, with the maximum speed for the fourth spiral mode being only $C_c \approx -9.0$.

We conclude this section with a presentation of disturbance temperature and disturbance velocity vector fields for $Pr = 4.35$ at $\eta = 0.6$. The evolution of these fields projected onto a meridional section over one vertical wavelength are displayed in figures 12 and 13. The vertical wavelengths in each frame have been scaled to a

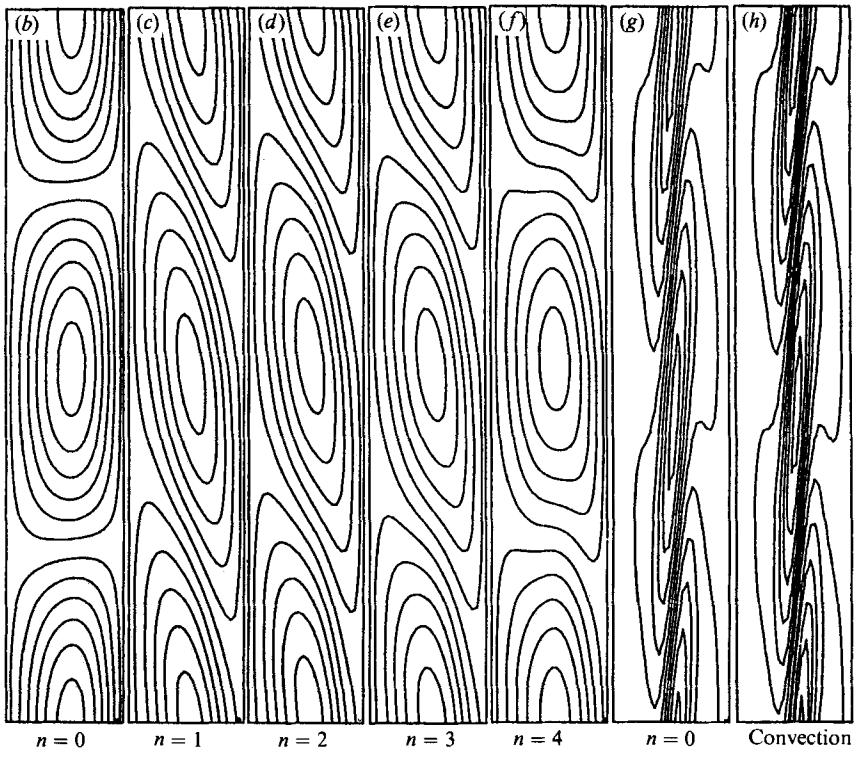


FIGURE 13. Evolution of the disturbance temperature contours in a meridional section at instability for $\eta = 0.6$ and $Pr = 4.35$. The left wall of each figure locates the outer cylinder. See caption of figure 12 for critical conditions.

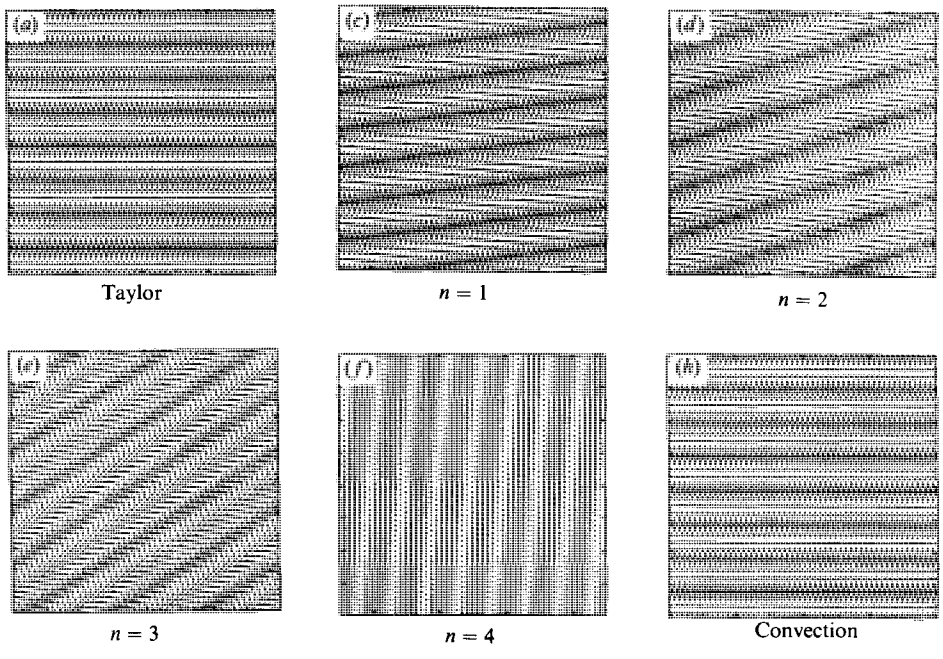


FIGURE 14. Evolution of disturbance velocity vector field projected on a cylindrical plane very near the outer cylinder for $\eta = 0.6$ and $Pr = 4.35$. See caption of figure 12 for critical conditions.

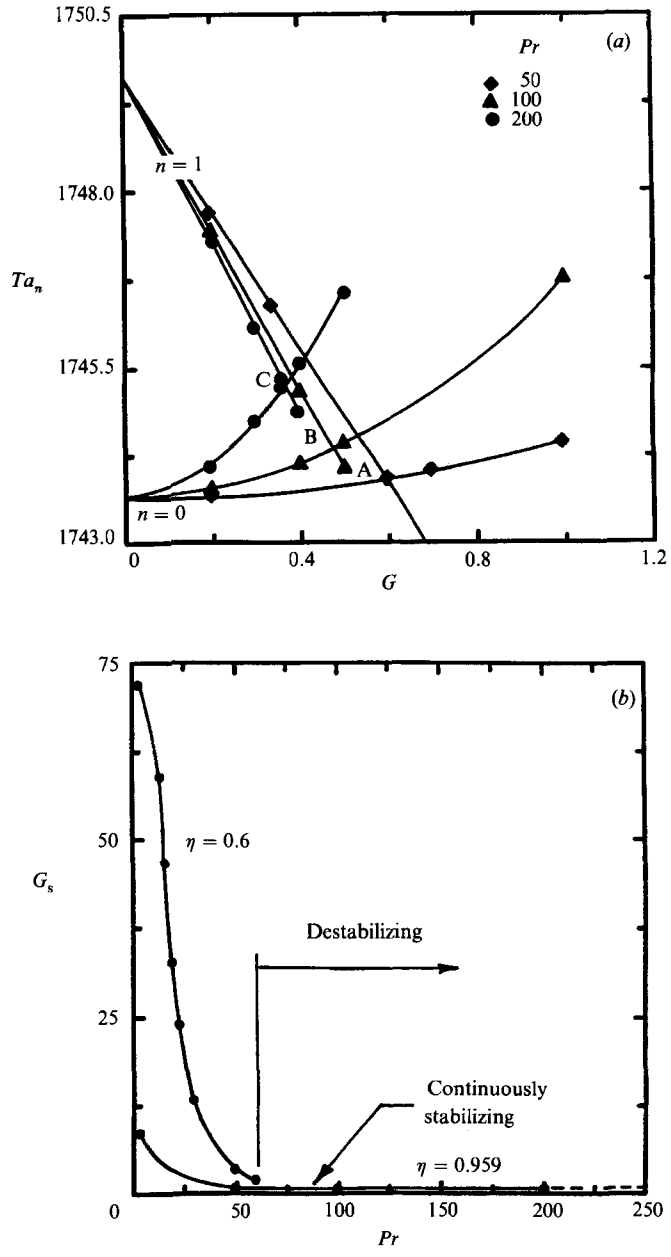


FIGURE 15. (*a*) Small-Grashof-number stability boundaries for the axisymmetric mode and the first asymmetric mode at $\eta = 0.959$ for selected Prandtl numbers. The region of Grashof stabilization of isothermal Taylor vortices is given by the intersection of the mode boundaries at points A, B and C where the destabilizing $n = 1$ modes supercede the stabilizing $n = 0$ modes. (*b*) Region of Grashof-number stabilization ($G_s$) of isothermal Taylor vortices for wide and narrow gaps as a function of the Prandtl number. For the wide gap at $\eta = 0.6$ Taylor vortices are destabilized for $Pr > 63.5$.

common height for ease of comparison. In the velocity vector fields portrayed in figure 12 the Grashof number increases from left to right following the evolution from isothermal Taylor cells through six examples of mixed convection to the final frame for pure convection. The intervening spiral modes exhibit skewed and overlapping

cells with the top of every cell tilted radially outwards. Figure 13 shows the evolution of disturbance temperature contours exactly out of phase with their disturbance velocity counterparts in figure 12. (Note the omission of the first frame corresponding to isothermal Taylor cells.) The neatly stacked temperature cells in figure 13(*b*) for slightly heated Taylor flow become skewed and slightly overlapping through the spiral modes. The strong temperature gradients at the gap centre in figure 13(*g*, *h*) is a manifestation of the shear-driven instability to which these axisymmetric modes correspond. In figure 14 cylindrical projections of disturbance velocity vector fields around the entire circumference of the annulus calculated at a radial point very close to the outer cylinder are displayed. The equal vertical and horizontal scales in this presentation exhibit the true inclination of the phase lines. Note the steep inclination of the fourth spiral mode in figure 14(*f*) just prior to the transition to horizontal convection cells figure 14(*h*).

### 4.3. *Stabilization of isothermal Taylor vortices*

Motivated by apparent discrepancies between the experiments of Snyder & Karlsson (1964) and Sorour & Coney (1979) we have conducted a parameter study of the effects of Prandtl number on the stabilization of Taylor vortices induced by radial heating. The $n = 0$ results in tables 1(*a–c*) and figure 6 show that isothermal Taylor cells for $\eta = 0.6$ are stabilized by radial heating at $Pr = 4.35$ and 15, but destabilized at $Pr = 100$. To elucidate these effects further, stability boundaries at three elevated Prandtl numbers at low Grashof number for the axisymmetric and first asymmetric modes in the narrow gap are presented in figure 15(*a*). We define the region of Taylor vortex stabilization by the Grashof number $G_s$ for which the quantity $[Ta_c - (Ta_c)_0]$ is maximum. According to this definition $G_s$ depends on the location of a maximum in the stabilizing $n = 0$ branch, or on the intersection of that branch with a destabilizing $n = 1$ branch as is the case at points A, B, and C in figure 15(*a*). Here it may be seen that the region of stabilization shrinks with increasing Prandtl number, but there is no evidence to suggest that destabilization will occur since the origin of the destabilizing mode is permanently fixed to a Taylor number above $(Ta_c)_0$ and the stabilizing axisymmetric-mode branches steepen continuously with increasing Prandtl number. A similar study was made for $\eta = 0.6$ and results for both radius ratios are presented in figure 15(*b*). Values of $G_s$ for $\eta = 0.6$ are due to intersections of the $n = 0$ and $n = 1$ branches at low $Pr$ and to maxima in the $n = 0$ branches at high $Pr$. The curves in figure 15(*b*) show that for both gaps the extent of Grashof stabilization decreases with increasing Prandtl number. Computations for $\eta = 0.6$ reveal that Taylor vortices are stabilized by radial heating at least in the range $4.35 \leqslant Pr \leqslant 63.5$ but destabilized for $Pr > 63.5$. For $\eta = 0.959$ stabilization is ensured for $4.35 \leqslant Pr \leqslant 200$, and since above $Pr = 200$ there are no additional mechanisms apart from centripetal and buoyancy forces to alter the character of the stability curves in figure 15(*a*), it is inferred that radial heating stabilizes Taylor vortices for all $Pr \geqslant 4.35$. The results in figure 15(*b*), however, show that the range of stabilization for the narrow gap becomes vanishingly small as $Pr \to \infty$.

## 5. Comparison with experiment

### 5.1. *The experiment of Snyder & Karlsson*

Snyder & Karlsson (1964) made careful measurements of the critical stability boundaries, wavenumbers, mode numbers and phase speeds with both positive and negative radial temperature gradients applied across the gap of an annulus with

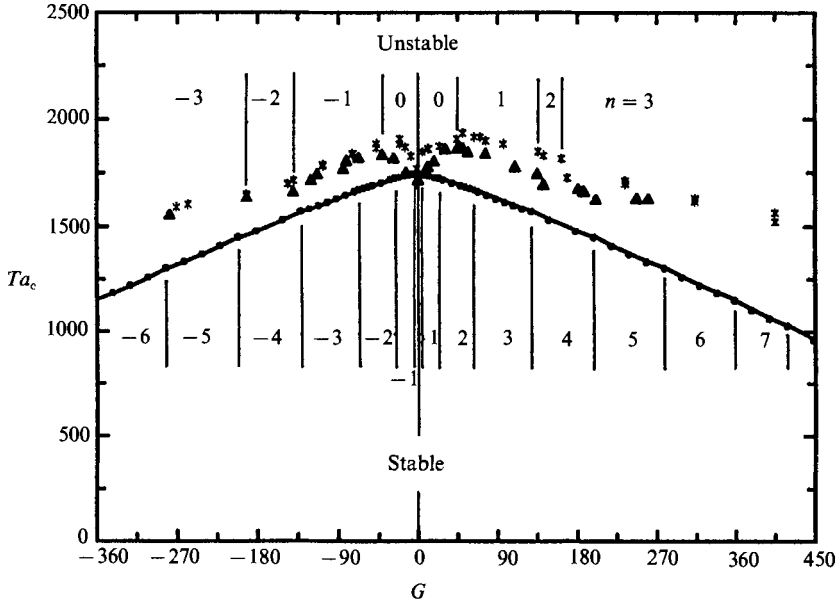


FIGURE 16. Comparison of the numerically computed infinite-aspect-ratio critical stability boundary (solid line) with the measured data (▲, *) of Snyder & Karlsson (1964) taken for $Pr = 5.77$, $\eta = 0.959$ and $\Gamma = 349$. Mode transition boundaries for the experiments are given above the data points and for the computations are given below the curve.

$\Gamma = 349$ and $\eta = 0.959$. A constant average Prandtl number was achieved by maintaining constant mean temperature ($T = 27.5\,^{\circ}\mathrm{C}$) for all experiments and uniformly heating one cylinder $\frac{1}{2}\Delta T$ above the mean and cooling the opposite cylinder $\frac{1}{2}\Delta T$ below. In the course of analysing their results, we discovered that the Prandtl number for water at the reported mean temperature was in error. The correct value is $Pr = 5.77$. The maximum Rayleigh number for these experiments is $(Ra)_{\max} \approx 1800$ which easily satisfies condition (1) for conduction-regime base flow in their large-aspect-ratio facility. The stability boundary obtained from new calculations performed for $Pr = 5.77$ at $\eta = 0.959$ are displayed as a solid line in figure 16 along with two sets of stability measurements by Snyder & Karlsson (1964). The experimentally observed transition boundaries between modes are indicated above the measured data points and the corresponding numerically computed transitions are indicated below the theoretical curve. Computed axial wavenumbers $K_c$ (discontinuous line curves) are compared with measured values (diamond symbols) at the onset of instability in figure 17 (*a*). The dimensional angular rotation rate of spiral disturbances in the numerical calculations are determined from the equation

$$\omega = \frac{-\sigma_i}{n(d^2/\nu)}. \tag{10}$$

In figure 17 (*b*) we compare computed (discontinuous curves) and measured (diamond symbols) critical angular velocities $\omega_c$ normalized by $\Omega_1$. The near-zero velocities for the weakly heated toroidal disturbances are omitted to facilitate a comparison of results on an enlarged scale. Both theory and experiment confirm that over a broad range of Grashof numbers the spiral disturbances rotate at very nearly $\frac{1}{2}\Omega_1$, which may be interpreted as the average angular velocity of the bounding cylinders.

In addition to the infinite-aspect-ratio idealization in the computations,

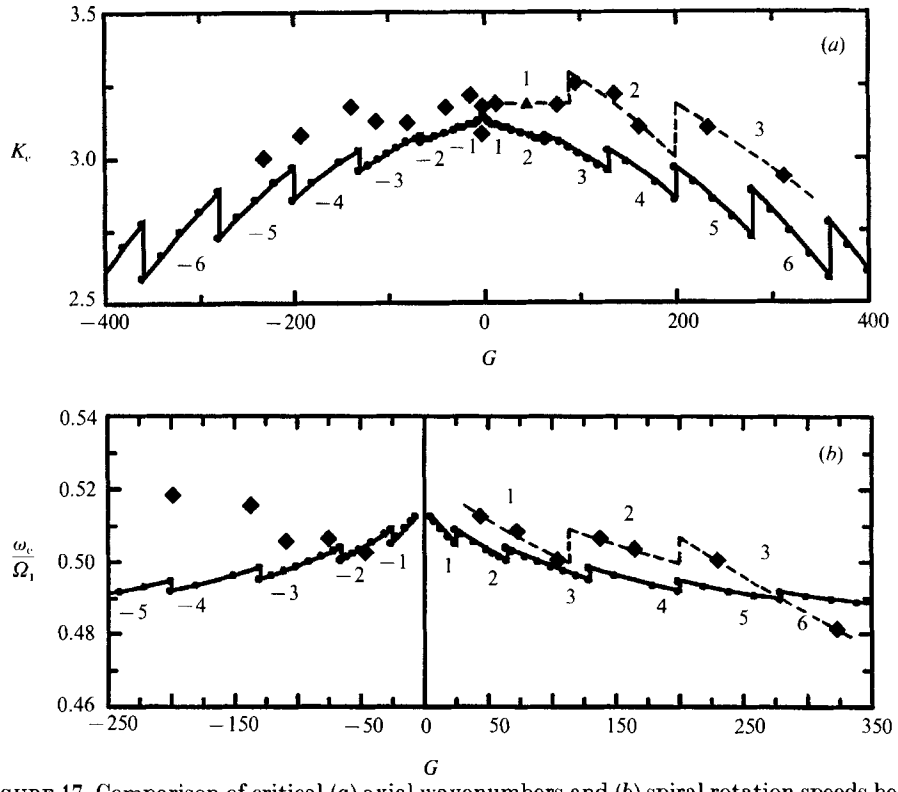


FIGURE 17. Comparison of critical (*a*) axial wavenumbers and (*b*) spiral rotation speeds between the numerically computed results for infinite-aspect-ratio (solid lines) and the measured data (solid diamonds) of Snyder & Karlsson (1964) taken for $Pr = 5.77$, $\eta = 0.959$ and $\Gamma = 349$. Note that the faired dashed lines through the experimental data for $G > 0$ exhibit a sawtooth behaviour similar to that found in the numerical calculations.

fundamental differences between the theory and experiment need mentioning. First, the experiments were attended by a small but finite density-stabilizing axial temperature gradient, whereas the stability calculations are for zero axial temperature gradient. Second, Snyder & Karlsson always observed an early transition to a weak cat's-eye instability with cells linked together vertically and centred at mid-gap. Bifurcation to fully developed toroidal and/or spiral cells filling the gap was observed as a second transition following the weak secondary cat's-eye motion. Third, Snyder & Karlsson observed spirals composed of counter-rotating cells of non-uniform width (cell-width ratio about 3:1). In a visualization study of radially heated Taylor–Couette flow in air with $\Gamma = 31.5$ and $\eta = 0.438$, Ball & Farouk (1989) report non-uniform cell widths in the same approximate ratio for counter-rotating toroidal vortices observed after transition from a spiral mode. Features of this type cannot be captured in the present analysis, which *a priori* incorporates a periodic disturbance function enforcing uniform width cells in each counter-rotating vortex pair.

In spite of the above differences, the measured and computed results exhibit remarkably similar behaviour. Snyder & Karlsson observed stabilization of the Taylor vortex mode up to $G \approx 50$ for negative radial temperature gradients and $G \approx -30$ for positive gradients. The present calculations also predict stabilization but only up to $|G| = 5.5$. The calculated r.m.s. deviation between measurement and

computation for the data plotted in figure 16 is 13.8%. Both experiment and theory exhibit the continuously destabilizing effect of the successively higher mode numbers that come into play with increasing values of $|G|$. The enhanced stability of the measurements relative to the numerically computed stability boundary may be attributed, at least in part, to the stable density stratification which accompanied their experiments. Although the calculated mode numbers are everywhere approximately double those observed in the experiments, favourable agreement between theoretical and experimental axial wavenumbers in figure 17(*a*) is observed. The r.m.s. deviation between experiment and theory for the wavenumber data is 4.4%. Good agreement between the measured and computed spiral rotation speeds in figure 17(*b*) is also apparent, the r.m.s. deviation being only 2.0%. Moreover, the dashed lines faired through the experimental data at positive values of $G$ in figures 17(*a*) and 17(*b*) reveal the same sawtooth transition behaviour observed in the numerical calculations. Finally, it is to be noted that the four types of helical disturbances depicted in figure 3 are in one-to-one correspondence with the observations of Snyder & Karlsson (1964) at the four combinations of radial heating and inner cylinder rotation listed in their figure 9.

### 5.2. *The experiment of Sorour & Coney*

Sorour & Coney (1979) reported relatively high-aspect-ratio ($\Gamma \approx 100$) stability measurements for two mineral (J. E. R. Coney, private communication) oils, in two-narrow gap geometries at $\eta = 0.911$ and $\eta = 0.948$ with inner cylinder rotating. These experiments were conducted by placing the apparatus in an oil bath whose temperature was carefully controlled. Increased radial heating was effected by raising the temperature of the bath and waiting until isothermal conditions were attained on each wall, the inner wall being cooler than the outer so that $G < 0$. A consequence of the experiment performed in this manner was that the average fluid temperature increased with increasing temperature contrast. Thus data points defining a stability curve at fixed $\eta$ each have a different Prandtl number. Measured values of the critical Grashof numbers, Taylor numbers, mean temperatures and temperature contrasts for the experiments are given in Sorour's (1977) Ph.D. thesis but thermal diffusivities were not reported. However, measured viscosity–temperature curves included in Sorour's thesis made it possible for engineers at Pen Rico Oil Company to identify the paraffinic oils and determine (we believe quite accurately) the temperature dependence of missing fluid properties. A listing of non-dimensional parameters calculated for these experiments is given in Ali (1988). The results show that the Prandtl number for $\eta = 0.948$ decreases significantly with increasing $|G|$, yielding variations over the range $300 \leqslant Pr \leqslant 500$ for 'oil A' and $500 \leqslant Pr \leqslant 860$ for 'oil B'. Critical wavelengths were not reported but flow visualizations were made to ascertain the mode of instability.

Only the results for $\eta = 0.948$ are considered here since this radius ratio is most akin to that in the experiments of Snyder & Karlsson (1964). For these data we find $(Ra)_{\max} \approx 1000$ and condition (1) ensures that the base flow was in the conduction regime. Figure 18 shows the experimental (dashed lines) and computed (solid lines) critical stability boundaries for these high-Prandtl-number fluids. One immediately notes the very small range of Grashof numbers covered by the experiments. It should be emphasized that computations were made for each specific parameter pair $(G, Pr)$ associated with each measured data point. Sorour & Coney report having observed only axisymmetric cells in their experiments for both oils. The stability calculations corroborate this result for oil B, but exhibit a critical stability boundary for oil A

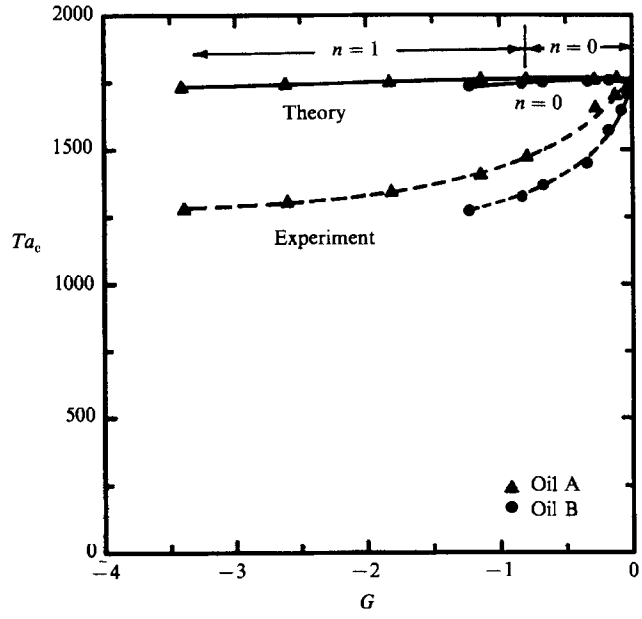


FIGURE 18. Comparison of the numerically computed infite-aspect-ratio neutral stability boundaries (solid lines) with the variable-Prandtl-number measurements (dashed lines, $n = 0$) of Sorour & Coney (1979) taken for two different oils at $\eta = 0.948$ and $\Gamma = 102$. The Prandtl-number variations in the experimental data are determined to be $300 \leqslant Pr \leqslant 500$ for 'oil A' and $500 \leqslant Pr \leqslant 860$ for 'oil B'.

composed of both $n = 0$ and $n = 1$ modes. The transition occurs at the third computed point near $G = -0.8$. Agreement with the experimental results of Sorour & Coney (1979) is less favourable than with the experiments of Snyder & Karlsson (1964). The r.m.s. deviation between computation and experiment is 22.2% for oil A and 23.4% for oil B. The measured stability boundaries are initially strongly destabilizing with respect to the critical value $(Ta_c)_0 = 1758$. The computed boundaries also exhibit destabilization, but only very weakly so. It is inferred from the narrow-gap-parameter study in figure 15(*b*) that destabilization of Taylor cells in the numerical calculations is due solely to variable Prandtl-number effects when $\mathrm{d}Pr/\mathrm{d}|G| < 0$. If the data possessed Prandtl-number variability of the form $\mathrm{d}Pr/\mathrm{d}|G| \geqslant 0$, a weak stabilization of Taylor cells would be computed. Some qualitative agreement may be found in the fact that the stability boundary for oil B lies below the boundary for oil A in both theory and experiment.

In contrast with the results in figure 16, the measured data of Sorour & Coney in figure 18 lie below the numerically computed stability boundaries. It is difficult to explain why the computations yield results decidedly more stable than Sorour & Coney's measurements. The fundamental difference between theory and experiment in both comparisons lies in the infinite-aspect-ratio and constant-fluid-property idealizations built into the linear stability analysis. While the aspect ratios in each experiment were large, the facility employed by Snyder & Karlsson had an aspect ratio 3.5 times that of Sorour & Coney. To compare fluid property variability in the experiments, we have calculated the maximum Prandtl-number variation across the gap. The maximum variation in Prandtl number in the experiments of Snyder & Karlsson was 15% while that for Sorour & Coney's experiment was 40%. The

relative importance of these differences, or even the direction in which they might displace a stability boundary, is not easy to assess.

## 6. Discussion and conclusion

The primary results of this investigation are the stability boundaries displayed in figures 6 and 7. Since the ordinate $Ta_c$ and the abscissa $G$ are both independent of the thermal diffusivity $\alpha$, the influence of $\alpha$ is directly observed through variation of the Prandtl number in these figures. The fundamental conclusion is that increasing the Prandtl number decreases system stability. In figure 8 the radius ratio $\eta$ appears both implicitly in the definition of $Ta_c$ and explicitly as a parameter. This radius-ratio-dependent Taylor number provides a relatively good collapse of the numerical results for $Pr = 4.35$ and $Pr = 100$, but does not show explicitly how the radius ratio affects system stability. In Ali (1988) the direct influence of $\eta$ is seen in a plot of the radius-ratio-independent Taylor number $T_c = (\Omega_1 d^2/\nu)^2$ versus Grashof number. That stability diagram shows unequivocably that increasing $\eta$ markedly decreases system stability, primarily by reducing $T_c$ across the entire range of radial heating.

A second important finding in this study are the $S^{c/r}(\Omega)$ and the $S^{c/r}(\Delta T)$ symmetries depicted in figure 3 which confirm the four combinations of spiral mode instability reported by Snyder & Karlsson for a stationary outer cylinder. Two analogous symmetries for a rotating outer cylinder with stationary inner cylinder may be derived following the procedures outlined in §3.3. It is anticipated that these symmetries will be consistent with the remaining types of spiral instability arising from the four combinations of outer-cylinder rotation and radial heating listed in figure 9 of Snyder & Karlsson (1964).

The dramatic increase in the number of critical spiral modes from $n_{max} = 4$ at $\eta = 0.6$ to $n_{max} \approx 50$ at $\eta = 0.959$ can be shown to be purely a geometrical effect if one assumes that the wavelengths of the spiral modes scale with the gap width $d$. In the limit that the spirals tilt 90° from horizontal, the maximum number of spiral modes which can be packed around the annulus is

$$n_{max} = \mathrm{INT}\left(\frac{2\pi}{\lambda_c(1-\eta)}\right), \tag{11}$$

where $\lambda_c$ is the critical wavelength calculated from equation 7($b$) at the outer cylinder wall. For both the wide and narrow gaps $\lambda_c \approx 2$ for Taylor vortices, and if one assumes that this scaling holds for the vertically oriented spirals as well, (11) gives $n_{max} = 8$ for $\eta = 0.6$ and $n_{max} = 77$ for $\eta = 0.959$. These values have the correct order of magnitude but the maximum number of critical modes is overestimated in each case. This means that the assumption $\lambda_c \approx 2$ for the terminal spiral modes is incorrect, as may be seen in figure 10. The terminal spiral wavelengths are more closely $\lambda_c \approx 4$ for $\eta = 0.6$ and $\lambda_c \approx 3$ for $\eta = 0.959$. In any event, $\lambda_c$ is still an $O(1)$ parameter and the above argument shows that the increase in the maximum number of critical modes with increasing radius ratio is simply a consequence of wave-fitting around the annulus.

The effect of radial heating on the relative stability of isothermal Taylor vortices has been determined for the two gaps over a range of Prandtl numbers. For $\eta = 0.6$ in the range $4.35 \leqslant Pr \leqslant 63.5$, Taylor vortices are stabilized by radial heating but destabilization occurs when $Pr > 63.5$. For $\eta = 0.959$ stabilization is ensured for $4.35 \leqslant Pr \leqslant 200$. In this latter case it is inferred that radial heating stabilizes Taylor

vortices for all $Pr \geqslant 4.35$, but the extent of Grashof stabilization tends to zero asymptotically as $Pr \to \infty$.

The comparisons with laboratory measurements are considered favourable when one considers the infinite-aspect-ratio, uniform-cell-width, and constant-fluid-property assumptions of the linear stability calculations. R.m.s. deviations between numerical calculation and experimental measurement of critical stability boundaries are about 14% for Snyder & Karlsson (1964) and 23% for Sorour & Coney (1979). Corroboration with Snyder & Karlsson's wavenumber and angular phase speed measurements is much better, the r.m.s. deviations being 4.4% and 2%, respectively. Even the detail of the sawtooth transitions is evident in the measured data in figure 17, attesting to the care taken by the investigators in an experiment performed over twenty-five years ago. The primary thing to learn from the experiments is that in finite-aspect-ratio systems there is substantial mode-number stabilization. In both experiments fewer unstable modes over comparable ranges of Grashof number are found. The rule of thumb for the comparison with Snyder & Karlsson (1964) is that half the number of critical spiral modes calculated by the infinite-aspect-ratio theory are found in the experiment at either positive or negative Grashof number. This strongly suggests that the slightly supercritical flow in the experiments has actually experienced a subharmonic bifurcation. Another important distinction not captured by linear stability theory is the non-uniform width of the counter-rotating cells that comprise a single spiral wavelength. There is mounting evidence that a common stable configuration for heated spiral cells (Taylor 1923; Snyder & Karlsson 1964) and strongly heated toroidal cells (Ball & Farouk 1989) is the one for which the cell width ratio is approximately 3:1, with the wider cell having the same sense of vorticity as the base flow. The stable 3:1 cell width configuration could well be a direct consequence of the supercritical subharmonic bifurcation. Spiral cells spurned from thermal gradients are manifestly different from those arising in isothermal circular Couette systems with a net axial flow through the annulus. In the latter case Snyder (1962) has shown that the two cells which make up a disturbance wavelength are of equal width.

The results of this study clearly point out the limitations of using linear stability theory for mixed convection in a confined system. It appears that a complete finite-aspect-ratio Navier–Stokes simulation, perhaps one including temperature-dependent fluid properties, will be required to capture the full details of slightly supercritical instability in these complicated flows.

We are indebted to Professor Snyder who supplied his original laboratory data to facilitate our comparison with his measurements and for similar reasons the assistance of Professor Coney is also acknowledged. Dr McFadden kindly supplied the numerical codes and guided us in getting them running on our local mainframe computer. Discussions with Drs S. Mobbs, K. Ball and J. Hart significantly helped improve the final manuscript. Appreciation is extended to the Von Neumann Center for awarding free supercomputer time on the Princeton Cyber 205. One of the authors (P.D.W.) is particularly grateful to the UK Science and Engineering Research Council for a Visiting Fellowship during the final stages of manuscript preparation. P.D.W. also acknowledges the gracious hospitality of the School of Mathematics at the University of East Anglia and especially that of his host and colleague Professor N. Riley.

## REFERENCES


ALI, M. E. 1988 The stability of Taylor–Couette flow with radial heating. Ph.D. thesis, University of Colorado, Boulder, CO.

ANDERECK, C. D., LIU, S. S. & SWINNEY, H. L. 1986 Flow regimes in a circular Couette system with independently rotating cylinders. *J. Fluid Mech.* **164**, 155–183.

BAHL, S. K. 1972 The effect of radial temperature gradient on the stability of a viscous flow between two rotating coaxial cylinders. *Trans. ASME* E: *J. Appl. Mech.* **39**, 593–595.

BALL, K. S. & FAROUK, B. 1986 Numerical studies of mixed convection flows in the annulus between vertical concentric cylinders with rotating inner cylinder. In *Proc. Eight Intl Heat Trans. Conf., San Francisco* (ed. C. L. Tien, V. P. Carey & J. K. Ferrell), pp. 435–440. Hemisphere.

BALL, K. S. & FAROUK, B. 1987 On the development of Taylor vortices in a vertical annulus with a heated rotating inner cylinder. *Intl J. Num. Meth. Fluids* **7**, 857–867

BALL, S. K. & FAROUK, B. 1988 Bifurcation and phenomena in Taylor–Couette flow with buoyancy effects. *J. Fluid Mech.* **197**, 479–501.

BALL, K. S. & FAROUK, B. 1989 A flow visualization study of the effects of buoyancy on Taylor vortices. *Phys. Fluids* A **1**, 1502–1507.

BARRATT, P. J. & ZUNIGA, I. 1984 A theoretical investigation of Bénard–Couette instabilities in nematic liquid crystals. *J. Phys.* D: *Appl. Phys.* **17**.

BATCHELOR, G. K. 1954 Heat transfer by free convection across a closed cavity between vertical boundaries at different temperatures. *Qt. Appl. Maths* **7**, 209–233.

BECKER, K. M. & KAYE, J. 1962 The influence of a radial temperature gradient on the instability of fluid flow in an annulus with an inner rotating cylinder. *Trans. ASME* C: *J. Heat Transfer* **80**, 106–110.

CHANDRASEKHAR, S. 1961 *Hydrodynamic and Hydromagnetic Stability*. Oxford University Press.

CHOI, I. G. & KORPELA, S. A. 1980 Stability of the conduction regime of natural convection in a tall vertical annulus. *J. Fluid Mech.* **99**, 725–738.

COGNET, G. 1984 Les esapes ver la turbulence dans l'ecoulement de Couette–Taylor entre cylindres coaxiaux. *J. Méc. Theor. Appl. Numero special*, pp. 7–44.

DI PRIMA, R. C. & SWINNEY, H. L. 1981 Instabilities and transition in flow between concentric rotating cylinders. In *Hydrodynamic Instabilities and the Transition to Turbulence* (ed. H. L. Swinney & J. P. Gollub). Topics in Applied Physics, vol. 45, pp. 139–180. Springer.

ECKERT, E. R. G. & CARLSON, W. O. 1961 Natural convection in an air layer enclosed between two vertical plates with different temperatures. *Intl J. Heat Mass Transfer* **2**, 106–120.

GARG, V. K. 1981 Stability of developing flow in a pipe: non-axisymmetric disturbances. *J. Fluid Mech.* **110**, 209–216.

GARG, V. K. & ROULEAU, W. T. 1972 Linear spatial stability of pipe Poiseuille flow. *J. Fluid Mech.* **54**, 113–127.

HART, J. E. 1971 Stability of the flow in a differentially heated inclined box. *J. Fluid Mech.* **47**, 547–576.

KELLER, H. B. 1976 Numerical solution of two point boundary value problems. *SIAM Regional Conference Series in Applied Mathematics*, vol. 24.

KREITH, F. 1968 Convection heat transfer in rotating systems. *Adv. Heat Transfer* **5**, 129–251.

LEE, Y., KORPELA, S. A. & HORN, R. N. 1982 Structure of multicellular natural convection in a tall vertical annulus. In *Proc. 7th Intl Heat Transfer Conf. Munich*, vol. 2, pp. 221–226.

LEE, Y. N. & MINKOWYCZ, W. J. 1989 Heat transfer characteristics of the annulus of two-coaxial cylinders with one cylinder rotating. *Intl J. Heat Mass Transfer* **32**, 711–722.

MCFADDEN, G. B., CORIELL, S. R., BOISVERT, R. F. & GLICKSMAN, M. E. 1984*a* Asymmetric instabilities in a buoyancy-driven flow in a tall vertical annulus. *Phys. Fluids* **27**, 1359–1361.

MCFADDEN, G. B., CORELL, S. R. & BOISVERT, R. F., GLICKSMAN, M. E., FANG, Q. T. 1984*b* Morphological stability in the presence of fluid flow in the melt. *Metall. Trans.* **15A**, 2117–2124.

POWELL, M. J. D. 1970 *Numerical Methods for Nonlinear Algebraic Equations*. Gordon and Breach.

ROBERTS, P. H. 1965 The solution of the characteristic value problem. Appendix to: Donnelly, R. J. & Schwarz, K. W. Experiments on the stability of viscous flow between rotating cylinders. VI. Finite-amplitude experiments. *Proc. R. Soc. Lond.* A **283**, 531–556.

ROESNER, K. G. 1978 Hydrodynamic stability of cylindrical Couette flow. *Arch. Mech.* **30**, 619–627.

SCOTT, M. R. & WATTS, H. A. 1977 Computational solution of linear two point boundary value problems via orthonormalization. *SIAM J. Numer. Anal.* **14**, 40–70.

SINGER, P. H. 1984 Techniques of low pressure chemical vapor deposition. *Semiconductor Intl Denver*, May, 72–77.

SLATEC COMMON MATH LIBRARY, National Energy Software Center, Argonne National Laboratory, Argonne, IL, written by K. L. Hiebert, based on Powell, 1970.

SNYDER, H. A. 1962 Experiments on the stability of spiral flow at low axial Reynolds numbers. *Proc. R. Soc. Lond.* A **265**, 198–214.

SNYDER, H. A. & KARLSSON, S. K. F. 1964 Experiments on the stability of Couette motion with a radial thermal gradient. *Phys. Fluids* **7**, 1696–1706.

SOROUR, M. M. 1977 Hydrodynamic instability, with special reference to the effect of heat transfer, in a concentric annulus having an inner rotating wall. Ph.D. thesis, University of Leeds.

SOROUR, M. M. & CONEY, J. E. R. 1979 The effect of temperature gradient on the stability of flow between vertical concentric rotating cylinders. *J. Mech. Engng Sci.* **21**, 403–409.

SOUNDALGEKAR, V. M., TAKHAR, H. S. & SMITH, J. T. 1981 Effects of radial temperature gradient on the stability of viscous flow in an annulus with a rotating inner cylinder. *Warme Stoff.* **15**, 233–238.

SPARROW, E. M., MUNRO, W. D. & JONSSON, V. K. 1964 Instability of the flow between rotating cylinders: the wide gap problem. *J. Fluid Mech.* **20**, 35–46.

STUART, J. T. 1986 Taylor vortex flow: a dynamical system. *SIAM Rev.* **28**, 315–342.

TAYLOR, G. I. 1923 Stability of a viscous liquid contained between two rotating cylinders. *Phil. Trans. R. Soc. Lond.* A **223**, 289–343.

THOMAS, R. W. & VAHL DAVIS, G. DE 1970 Natural convection in annular and rectangular cavities: a numerical study. *Proc. 4th Intl Heat Transfer Conf., Paris, paper* NC 2.4.

VAHL DAVIS, G. DE & THOMAS, R. W. 1969 Natural convection between concentric vertical cylinders. *Phys. Fluids Suppl. II*, 198–207.

VIVES, C. 1988 Effects of a forced Couette flow during the controlled solidification of a pure metal. *Intl J. Heat Mass Transfer* **31**, 2047–2061.

WALOWIT, J., TSAO, S. & DI PRIMA, R. C. 1964 Stability of flow between arbitrarily spaced concentric cylinder surfaces, including the effect of a radial temperature gradient. *Trans. ASME* E: *J. Appl. Mech.* **31**, 585–593.

WEIDMAN, P. D. 1989 Experimental techniques in laboratory rotating flows. In *Frontiers in Fluid Mechanics* (ed. M. Gad-El-Hak). Lecture Notes in Engineering, vol. 45. Springer.

WEIDMAN, P. D. & ALI, M. E. 1989 The stability of Taylor–Couette flow with radial heating. In *Proc. 2nd Workshop on Instabilities and Nonequilibrium Structures, Universidad de Santa Maria, Valpariso, Chile, Dec. 17–22, 1987.* Reidel.

WEIDMAN, P. D. & MEHRDADTEHRANFAR, G. 1985 Instability of natural convection in a tall vertical annulus. *Phys. Fluids* **28**, 776–787.

YIH, C.-S. 1961 Dual role of viscosity in the stability of revolving fluids of variable density. *Phys. Fluids* **4**, 806–811.